Rock Mechanics and Rock Engineering (2019) 52:1723–1743
https://doi.org/10.1007/s00603-019-1739-7

ORIGINAL PAPER

Scaling of Fracture Patterns in Three Deep Boreholes and Implications for Constraining Fractal Discrete Fracture Network Models

Mohammad Javad Afshari Moein[1] · Benoît Valley[2] · Keith F. Evans[3]

Received: 15 May 2018 / Accepted: 17 January 2019 / Published online: 25 January 2019

Abstract

We present a methodology for generating fractal fracture networks in one, two and three dimensions that respects the dual power-law model, in which the scaling characteristics are set by the two independent parameters: (1) the correlation dimension that pertains to separation of fracture centers, and (2) the length exponent that governs the distribution of fracture lengths. Synthetic fracture distributions were generated to evaluate the stereological relationships between the scaling parameters of 2D and 3D networks, and the scaling of fracture intersection points along a scanline through the network. The results showed that it is not possible to estimate the 2D and 3D fractal scaling parameters of the correlation dimension from the 1D correlation dimension of fracture spacing from scanlines through the network, even if the length exponent is known a priori. Synthetic 1D distributions of fracture spacing of known correlation dimension were used as a benchmark to test the consistency of estimates of fractal dimension derived from box-counting, two-point correlation, and power-law fitting. The results showed that the correlation dimension obtained from the two-point correlation method provided the most stable and reliable estimate of the fractal dimension of fractures on 1D scanlines or boreholes. Application of the two-point correlation function to the observed fracture distributions along three deep boreholes in crystalline rock at Basel, Switzerland and Soultz-sous-Forêts, France showed that the distribution was fractal over more than two orders of magnitude in scale, and in all cases the fractal dimensions was in the range 0.86–0.88. Similar results were obtained for fracture sets of common orientation within the wells, although the fractal dimension ranged between 0.65 and 0.75. This constitutes strong evidence that fracturing in rock masses penetrated by the wells follows a fractal organization.

Keywords Discrete fracture networks (DFN) · Fracture spacing · Power-law scaling · Deep boreholes · Fractal geometry

List of symbols

D	Correlation dimension
a	Fracture length exponent
r	Distance between fracture centers (m)
l	Fracture length (m)
$C(r)$	Correlation function
$N_p(r)$	Number of pairs of fractures whose center-to-center distance is less than r
N_t	Total number of fractures
L	Domain length in 1D, 2D and 3D (m)
m	Number of equal-sized sub-domains in a Multiplicative Cascade process
l_{min}	Minimum fracture length (m) in DFN generation
l_{ratio}	The ratio of sub-domain side length to the domain side length in Multiplicative Cascade process
P	Probability of having a fracture in a sub-domain in Multiplicative Cascade process
U	Fracture assignment vector
CumP	Cumulative probability density vector
t	Ruler length in 1D box-counting technique
$N_b(t)$	Number of rulers of length t containing at least one fracture
D_b	Box-dimension
s	Fracture spacing

✉ Mohammad Javad Afshari Moein
mohammad.moein@erdw.ethz.ch

[1] Engineering Geology, Department of Earth Sciences, Geological Institute, ETH Zürich, Sonneggstrasse 5, 8092 Zurich, Switzerland

[2] Center for Hydrogeology and Geothermics, University of Neuchâtel, Rue Emile-Argand 11, 2000 Neuchâtel, Switzerland

[3] Geothermal Energy and Geofluids, Department of Earth Sciences, Institute of Geophysics, ETH Zürich, Sonneggstrasse 5, 8092 Zurich, Switzerland

N_s Number of spacings greater than or equal to a specific spacing s
D_s Power-law exponent of fracture spacing
κ Fischer coefficient

1 Introduction

Enhanced Geothermal Systems (EGS) aim to extract the heat from the earth by circulating fluids (e.g., water) between injection and production wells drilled into sufficient depth to reach temperatures higher than 150 °C. Outside of areas of recent volcanism, the target reservoirs tend to be found in low-porosity basement rocks, where natural flow occurs primarily through the fracture network (Genter et al. 2010; Gillespie et al. 1993). The natural fracture transmissivity is usually insufficient to allow economical flow rates, and thus must be enhanced. This is typically accomplished by performing massive fluid injections into the reservoir to increase the permeability of the fractured media, a process referred to as hydraulic stimulation. The mechanisms underlying the process are complex and not fully understood. However, evidence suggests that shearing of rough-walled fractures resulting from effective stress changes in response to the increased pore pressure plays a role in increasing fracture permeability (Evans et al. 2005; Evans 2005). The elevated pore pressure can also generate new fractures. Hydraulic shearing/fracturing is commonly accompanied by microseismic activity, and some events may be large enough to be felt. The public fear of induced damaging earthquakes has led to project curtailment in some cases, such as occurred in the Basel and St. Gallen geothermal projects in Switzerland. Thus, the major challenge in developing geothermal resources is to enhance the permeability of the target reservoir adequately through hydraulic stimulation without inducing damaging seismicity.

To design and assess EGS development strategies, a geological model of the target rock mass is required. This geological model should be representative of the whole reservoir with a realistic representation of relevant geological attributes such as the fracture network geometry from small to large scales. The characterization of the fracture network is especially challenging at early project stages when data from only a single exploration well penetrating the target reservoir may be available.

Since the deterministic characterization of fracture network in deep reservoirs is not yet possible, stochastic realizations, referred as discrete fracture networks (DFN), conditioned by statistical parameters that are amenable estimation are widely used to generate fractures within the rock mass, perhaps supplemented by deterministic fractures at the wellbore where direct observations are available. DFN models have been widely used to simulate the geomechanical and hydrological behavior of fractured rocks in many engineering applications, such as radioactive waste disposal, EGS developments, underground construction, hydraulic fracturing in shale gas exploitation (Lei et al. 2017 and references therein). However, the fracture length distribution in DFN models, which is a key parameter that influences the connectivity of the fracture network, is particularly difficult to constrain from borehole observations alone.

Fracture network characteristics have been studied from outcrops and multi-well study sites, where a more complete characterization of the fractures is possible (Cowie et al. 1996). In such situations, it has been observed that several attributes of fracture networks exhibit power-law patterns referred to as fractal organization (e.g., Barton 1995; Bonnet et al. 2001; Bour et al. 2002; Davy et al. 1990; de Dreuzy et al. 2002; Lei et al. 2015; Odling et al. 1999). Specifically, power-law scaling has been applied to characterize spatial distribution, trace length, spacing, RQD [Rock Quality Designation, Deere and Deere (1988)], aperture, surface roughness etc. (e.g., Barton and Zoback 1992; Boadu and Long 1994; Bonnet et al. 2001; Power and Tullis 1991), that influence the connectivity of fractured rocks (e.g., Alghalandis et al. 2015; Darcel et al. 2003c). Fractal DFNs consider fractures of all scales leading to a more representative model of the target rock mass (Davy et al. 2018). The origin of the prevalence of power-law scaling in nature is not entirely clear, although several researchers have proposed the implied statistical scaling is a facet of the behavior of complex self-organized critical dynamics (Allegre et al. 1982; Bak et al. 1988; Sornette 2006; Sornette et al. 1990). Davy et al. (2010) and Spyropoulos et al. (2002) have shown that the stress interactions between fractures in a growing fracture population can lead to power-law distributions. This suggests that some relations exist between the characteristics of the fracture network and the stress variability within this fractured rock mass. In the special case when a single fracture is present, the size of the stress perturbation scales linearly to the size of the fracture inducing the perturbation (Eshelby 1957; Pollard and Segall 1987). However, for a fracture network, the interrelationship between stress and fractures becomes non-trivial (Valley et al. 2014). Nevertheless, studies of near-continuous profiles of borehole failure suggests that stress fluctuations also follow power-law scaling (e.g., Day-Lewis 2008; Valley and Evans 2014). The relation between the power-law scaling of fracture networks and stress fluctuations are not well understood. Clarification of the potential relationship could have important practical implications, such as allowing constraints to be placed on attributes of the fracture network such as fracture length distribution that are otherwise hard to quantify by observation of stress fluctuations from borehole failure. In this regard, Afshari Moein et al. (2018a) have proposed stress-based tomography, which uses stress fluctuations along

the boreholes to infer a probabilistic image of the fracture network.

Further applications could also be envisaged if a clear link could be established between power-law scaling of fracture attributes and the seismogenic b-value parameter that relates the earthquake frequency and magnitude. Alghalandis et al. (2013) have explored the possibility of extracting the fracture network geometry from induced seismicity in a geothermal project in the Cooper Basin of South Australia. Afshari Moein et al. (2018b) have also found similarities between the scaling properties of induced seismicity patterns and fracture network. These similarities led to a statistical seismicity model that could forecast the maximum magnitude in hydraulic stimulation as a function of perturbed volume based on clustering and size distribution of early events.

Despite the recent advances, a physical linkage between scaling properties of key reservoir characteristics such as fracture network, stress fluctuations and microseismic frequency size distribution is still lacking (Afshari Moein 2018). A necessary step towards establishing potential relationships is to improve our understanding of the characteristics and limitations of the scaling laws in each discipline. In this paper, our principal aim is to clarify the scaling properties of 1D fracture spacing data from three deep boreholes. Pursuant to this, 1D synthetic fracture spacing data were generated to identify the best methodology for characterizing the scaling properties of borehole data. Then, we explore the possibility of using 1D fracture spacing data obtained from boreholes to constrain 2D and 3D structural models of the rock mass. Finally, we outline the scaling characteristics of natural fractures derived from borehole images of two geothermal reservoirs of Basel and Soultz-sous-Forêts, and discuss the potential implication of the scaling relationships.

2 Scaling of Fractures in 2D from Synthetic Networks

2.1 Synthetic Fracture Network Model

To analyze the limitations of line sampling and power-law scaling of borehole data and possible extrapolation to a 3D geological model, a discrete fracture network model with valid stereological relationships is required. Discrete fracture networks (DFN) are geometrical representations of fracture attributes derived using stochastic methods and computational tools. The only DFN model we are aware of that respects stereological relationships is a dual-power-law model proposed by Davy et al. (1990) that is based upon Eq. (1), below. Here, we begin by presenting a step-by-step methodology for generating a DFN that respects this equation. The DFN model generated from the Eq. (1) that links the fractal spatial patterns of fractures to power-law distributions of fracture length and fracture centers given by:

$$n(l, L)\mathrm{d}l = \alpha \cdot L^{\mathrm{D}} l^{-a}\mathrm{d}l, \quad l \in [l_{\min}, l_{\max}] \tag{1}$$

Here, $n(l,,L)\mathrm{d}l$ is the number of fractures whose length is in the range $[l,\ l+\mathrm{d}l]$ and whose centers belong to a cubic volume in three dimensions of side length L, α is a constant related to the fracture density, D is the correlation dimension of fracture centers, and a is the length exponent. Many researchers have applied this model to study hydraulics and mechanics of fractal DFNs (e.g., Harthong et al. 2012; Kim 2007; Lei and Gao 2018; Verscheure et al. 2012). As an example, when $a = D + 1$, the DFN generated is self-similar and the connectivity of the network is scale invariant (Darcel et al. 2003c). Bour et al. (2002) applied this statistical model to evaluate scaling inherent in the fracture network geometry of multiscale fracture maps taken from outcrops in the Hornelen basin (Norway). The dual power-law model contains no direct relationship between first-order descriptors, such as D and a and hence it is referred to as a first-order model. Bour and Davy (1999) present a second order relation in which the exponents, D and a are related by $x = \frac{a-1}{D}$, where x is the exponent of a power-law including the average distance d from a fracture to the closest fractures having a larger length (i.e., $d(l) \sim l^x$). Darcel et al. (2003a) introduced another scaling law for the Hornelen basin dataset that relates the length of a fracture to the mean distance from the fracture center to its nearest neighbor. They related this scaling law to the stress shadow which is present around large fractures. Davy et al. (2010) extended the theory to address the problem of fracture intersections and proposed some simple rules that are not present in the first-order model. In this paper, we use the initial form of the dual power-law model without any modifications. Values of the two power-law indices, D and a, will be limited to ranges suggested by extensive measurements published in the literature. Specifically, studies of 2D outcrops yield estimates for the correlation dimension D of between 1.3 and 2, and the length exponent a falls between 1.3 and 3.5 (Bonnet et al. 2001; Renshaw 1999). Unfortunately, no estimates of D and a for 3D networks are reported in the literature as there is no direct method to image 3D size distribution of fractures at depth.

Before presenting the DFN generation methodology, it is useful to clarify the available technique to compute the fractal dimension (D) of fracture patterns. Fractal geometry has been widely utilized to quantify the scaling properties of fracture networks (e.g., Chilès 1988; Davy 1993). For a detailed analysis of the scaling in fractured media, we refer to Bonnet et al. (2001). The spatial organization of fractures can be quantified by a box-counting technique (Allegre et al. 1982; Berkowitz and Hadad 1997; La Pointe 1988; Odling 1992) or two-point correlation function (Hentschel

and Procaccia 1983). The traditional box-counting technique is strongly affected by finite size effects, whereas the two-point correlation function is less affected and seems a better method to derive the scaling exponent of the spatial distribution of fracture centers in 2D fracture outcrops (Bonnet et al. 2001; Bour et al. 2002). We illustrate the differences in implementation of these techniques to 1D fracture patterns in Sect. 3. The two-point correlation function or correlation integral describes the spatial correlation of fracture centers, and is given by,

$$C(r) = \frac{2}{N_t(N_t - 1)} N_p(r) \sim r^D, \tag{2}$$

where N_t is the total number of fractures, N_p is the number of pairs of fractures whose center-to-center distance is less than r and $\frac{N_t(N_t-1)}{2}$ is the total number of pairs of fractures (Bonnet et al. 2001). The correlation dimension (D) can be determined by computing the local slope of the correlation function $C(r)$ in a log–log plot. The correlation function has been widely used by earth scientists to characterize the spatial distribution of micro-fractures in rock samples in granite and also earthquake hypocenters (Hirata et al. 1987). Here, we apply the concept of correlation function to: (1) validate our synthetic DFN generator and (2) analyze 1D fracture patterns in deep boreholes.

2.1.1 DFN Generation Methodology

Here, we briefly review and illustrate some DFN generation methodologies that can be found in the literature, and comment on their possible implications. The conventional Poisson DFN model, also known as the Baecher model, is an early DFN model developed to study the hydraulic and mechanical behavior of fracture networks (e.g., Baecher and Lanney 1978; Baghbanan and Jing 2007; Bour and Davy 1997; de Dreuzy et al. 2001; Dershowitz and Einstein 1988). The concept behind the Poisson DFN model is to populate a medium with a random (uniform) distribution of fracture centers (Dershowitz et al. 1993). However, this model is not able to represent the tendency of fracture populations to display clustering at different scales. An alternative that does not suffer from this deficiency is the fractal fracture network approach that generates networks that capture the scaling and clustering seen in real fracture networks.

We found two methods to generate fractal fracture networks in the literature; (1) the Levy–Lee flight model and (2) Imposition of a power-law length distribution to a fractal spatial distribution of fracture centers generated by a multiplicative cascade process. The Levy–Lee flight process is a random walk method that generates fractal fracture networks by imposing power-law steps in random directions between 0° and 360° (Clemo and Smith 1997). The distance between two consecutive fracture centers is selected randomly from a power-law distribution with an exponent of D, and the fracture length is taken as proportional to the distance from the previous fracture. This methodology is implemented in the commercial software package Fracman (Dershowitz et al. 1993). Since the generation domain of a fracture network is limited, the consecutive fractures might extend outside of the 2D and 3D domain, and the fractal dimension (D) of the generated network will thus not necessarily correspond to the input fractal dimension (Darcel 2002). For this reason, we were unable to obtain an equivalence between output and input D when using the Levy–Lee fractal DFN generator.

The general methodology based on the Multiplicative Cascade process has already been described in different papers (e.g., Harthong et al. 2012; Verscheure et al. 2012), although details of its implementation are lacking. Thus, here we give a step-by-step description of the implementation we have used. This process includes both the generation of a fractal density distribution in a recursive operation of fragmentation and the allocation of a power-law length distribution, as given in Eq. (1). We begin by describing the methodology used to generate 2D fractal networks before progressing to cover 3D network generation.

2.1.2 2D Fractal DFN Generation

2.1.2.1 Initial Parameters The input parameters required to generate a 2D DFN are: domain length L, length exponent a ($a > 1$), correlation dimension of fracture centers D ($1 < D \leqslant 2$), fracture density constant α, and the minimum length of the fractures l_{min}. The latter is necessary to limit the number of iterations in the fractal density distribution and the total number of fractures N_t. We expect to have a power-law correlation function (Eq. 2) extending from the minimum length (e.g., 1 m) upwards over at least two orders of magnitude (100 m). The number of iterations n required to reach the degree of fragmentation set by the minimum length l_{min} is computed from:

$$l_{min} = \frac{L}{2^n} \tag{3}$$

Since we are defining the domain length (L) as one of the inputs of the DFN model, there is no constraint on the maximum fracture length l_{max} and it can vary depending on the length exponent a. The total number of fractures N_t can be calculated by integrating Eq. (1) over the fractures larger than the minimum length, as shown in Eq. (4).

$$N_t = \int_{l_{min}}^{\infty} n(l, L) \cdot \mathrm{d}l = \frac{\alpha}{a-1} L^D l_{min}^{-(a-1)} \tag{4}$$

2.1.2.2 Fractal Distribution of Density (Multiplicative Cascade Process) The fractal density distribution of fractures

of given fractal dimension D is generated using a so-called multiplicative cascade process applied to a domain whose size is L (e.g., Darcel et al. 2003c; Lovejoy and Schertzer 1986; Meakin 1991). The methodology we have implemented follows that outlined by Darcel et al. (2003c). To summarize, in the first iteration, the domain of size L is subdivided into m equal-sized sub-domains. Thus, the ratio of sub-domain side length to domain side length is $l_{\text{ratio}} = \sqrt{m}$. Then, n initial probabilities, P_i, are chosen that satisfy Eqs. (5) and (6),

$$\sum_{i=1}^{m} \frac{P_i^2}{\left(\frac{1}{l_{\text{ratio}}}\right)^D} = 1 \tag{5}$$

$$\sum_{i=1}^{m} P_i = 1 \tag{6}$$

In our implementation, we follow Darcel et al. (2003c) and take $l_{\text{ratio}} = 2$ and $m = 4$. The four probabilities are randomly assigned to each of the sub-domains. In the second iteration, each sub-domain (parent) is itself subdivided into four equal parts (offspring). The same four probabilities used in the first iteration are then multiplied by the probability of the parent sub-domain in question and the results randomly assigned to the four offspring sub-domains (Harthong et al. 2012; Verscheure et al. 2012). The process of division and assignment of permuted and multiplied probabilities is then repeated in subsequent iterations to produce a fractal probability map on the domain that has increasingly fine resolution. The map derived from Eqs. (5) and (6) defines the second order fractal spectrum of the probability field. For a detailed description on the multifractal spectrum of a DFN we refer to Bonnet et al. (2001) and Hentschel and Procaccia (1983). For n iterations, the Multiplicative Cascade process generates $2^n \times 2^n$ probabilities assigned to sub-blocks whose size from Eq. (3) is $l_{\min} = \frac{L}{2^n}$ (assuming $l_{\text{ratio}} = 2$). The fractal probability field generated in this way is taken as a proxy for the fractal fracture density distribution.

2.1.2.3 Assigning Random Fracture Centers According to Probability Maps Although the generation of fractal density distributions is well described in the literature (Darcel et al. 2003c; Harthong et al. 2012; Kim 2007), the further steps of populating a given probability density map with a realization of a random fracture network has not been described in detail. Thus, we provide a step-by-step description of the procedure we implemented in our DFN generator, which uses the discrete inverse transform method to extract random distributions from the probability density map. The procedure is illustrated in Fig. 1. We begin by writing the $[n \times n]$ probability density map as a $1 \times n^2$ probability density vector by concatenating successive columns, and then taking the cumulative sum of its elements to obtain the cumulative probability density vector *CumP*. The cumulative sum of the probability density vector is close, but not necessarily equal to unity due to computational inaccuracy in the multiplicative cascade process. Thus, *CumP* is normalized by the cumulative sum, giving a monotonically increasing series whose last element is unity, as shown in Fig. 1.

Now, a fracture assignment vector U containing N_t (the total number of fractures computed from Eq. 4) uniform random numbers between 0 and 1 is generated, where N_t is the total number of fractures to be used in populating the domain (Eq. 4). That is,

$$U = \left[u_1\ u_2\ u_3\ \ldots\ u_{N_t} \right] \tag{7}$$

The discrete inverse transform method is then used to map each element U_i of U to the closest matching element of *cumP* according to the inequality,

$$cumP_{j-1} \leqslant U_i < cumP_j \tag{8}$$

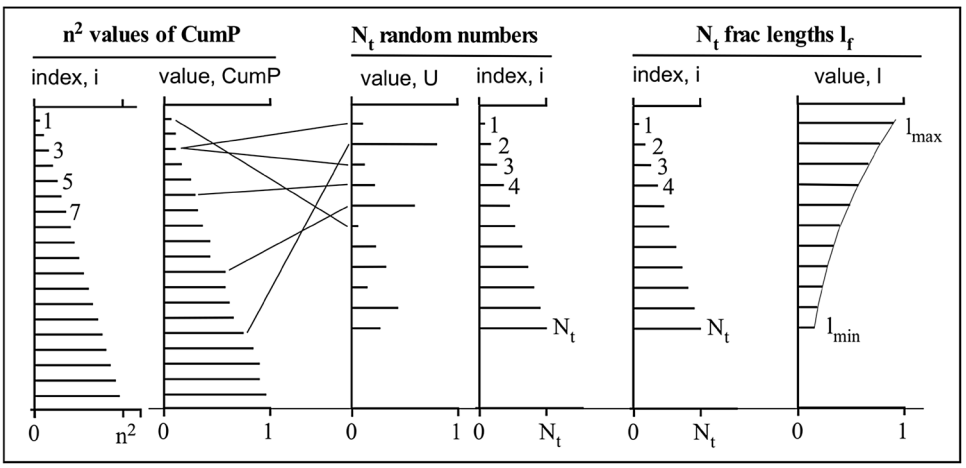

Fig. 1 Illustration of the procedure for populating the probability distribution map generated using the multiplicative cascade process with fracture centers, and then assigning a power-law length distribution to the fractures that is consistent with Eq. (13). The vector U in the center is the fracture assignment vector. This illustration corresponds to the classical approach to implement a heterogeneous Poisson point process (e.g., Moller and Waagepetersen 2003)

Thus, each element U_i of the fracture assignment vector U is associated with an element $cumP_j$ of $cumP$ (Fig. 1) and hence the corresponding cell of the probability density map. In this way, fracture centers are uniquely assigned to cells of the probability density map, although elements in U that have the same value will be mapped to the same cell. The specific distribution realized depends upon the random number set used to form U. The exact position of the fracture center within a cell is attributed randomly using a uniform probability over the cell.

2.1.2.4 Assigning a Fracture Length to Fracture Centers At this stage, U is the vector containing N_t random numbers and each random number represents a fracture that has been located inside the domain. We define a length vector l_f, written as in Eq. (9), whose N_t elements represent the lengths of each fracture written in descending order (i.e., $l_{f_1} > l_{f_2} > l_{f_3} > \cdots > l_{f_{N_t}}$)

$$l_f = \left[l_{f_1} \;\; l_{f_2} \;\; l_{f_3} \ldots \;\; l_{f_{N_t}} \right] \tag{9}$$

The index *fi* for each element of the length vector maps to the corresponding index i of the fracture assignment vector, U_i, and thus to locations on the probability density map (Fig. 1). The actual fracture lengths of the vectors l_f are assigned as follows. For a first-order model, the number of fractures having a length between l and $l + \mathrm{d}l$ is defined by Eq. (1). Therefore, the number of fractures whose length is greater or equal to a given length l' is given by,

$$\int_{l'}^{\infty} n(l, L) \cdot \mathrm{d}l = \int_{l'}^{\infty} \alpha \cdot L^D l^{-a} \cdot \mathrm{d}l = \frac{\alpha}{a-1} L^D l'^{-(a-1)} \tag{10}$$

Now, if we select the first fracture in the length vector whose length is l_{f_1} ($=l_{\max}$), the number of fractures greater than or equal to l_{f_1} is equal to 1. Therefore, substituting $l' = l_{f_1}$ into Eq. (10) and equating to unity gives:

$$\frac{\alpha}{a-1} L^D l_{f_1}{}^{-(a-1)} = 1 \tag{11}$$

Similarly, for any index i of l_f, the number of fractures whose length is greater than l'_{f_i} is i, and thus,

$$\frac{\alpha}{a-1} L^D l_{f_i}{}^{-(a-1)} = i \tag{12}$$

Rearranging Eq. (12) gives an expression for the length of each fracture, l'_{f_i}, in the length vector, l_f, as.

$$l_{f_i} = \left(\frac{\alpha}{a-1} \frac{L^D}{i} \right)^{\frac{1}{a-1}} \tag{13}$$

The described methodology of random DFN generation was implemented in a MATLAB script. An example of a fractal probability field generated in a domain of size $L =$ 500 m for a fractal dimension of $D = 1.5$ is presented in Fig. 2a. The number of iterations was set to $n = 6$, giving a minimum length, $l_{\min}$, of 7.8 m from Eq. (3). Finer density maps can be obtained by using a higher number of iterations. A realization of fractal DFN computed from the probability map using length exponent $a = 2$ is shown in Fig. 2b. The fracture density parameter, α, was taken as 1 so as to give approximately 1433 fractures. The fractal nature of the distribution of centers was verified by calculating the two-point correlation function of fracture centers $C(r)$ given by Eq. (2) for fracture separations, r, that were logarithmically uniformly spaced with 20 points for each order of magnitude up to the maximum separation of 500 m. The resulting correlation function is shown in Fig. 2c, together with the local slope of the log–log plot. The slope has a constant value of 1.5 over two orders of magnitude between $r = 1 - 100$ m, as expected for a fractal distribution of fractal dimension 1.5. The fractal nature of the length distribution is demonstrated in Fig. 2d which shows the logarithm of the number of fractures having a length greater or equal to l versus the logarithm of l. The data define a power-law with a slope of -1, consistent with expectations that the slope should be $1 - a$ (Bonnet et al. 2001).

2.1.3 Effect of Geometric Boundaries on 2D Fractal DFNs

Fractures in generated DFNs may extend outside the predefined domain (L). The application of such DFNs in any modeling scenarios requires a proper understanding of the possible effect of geometric boundaries. The specific geometric boundary implemented may alter the statistics of DFNs from the infinite domain case. In this section, we define two boundary treatment methods and apply them to various 2D DFNs to examine their effect. The first method completely removes those fractures that extend outside the domain length (L), and the second trims the fracture sections that protrude out of the domain with the consequence that the fracture centers of the trimmed fractures become repositioned within the domain.

Darcel et al. (2003b) have shown that the behavior of fractal DFNs broadly divides into two regimes with a transition at $a = 2$. We restrict our analysis to the two ranges that lie on either side of the transition and take the width of each range to be consistent with the range of values commonly reported for natural fracture networks. That is, we take $1.3 \leqslant a \leqslant 2$ and $2 < a \leqslant 3.5$. Higher values of the length exponent a correspond to a higher ratio of smaller to larger fractures. Thus, values of a that lie in the first range generate a greater proportion of large fractures than values that lie in the second range, and hence would be expected to have a

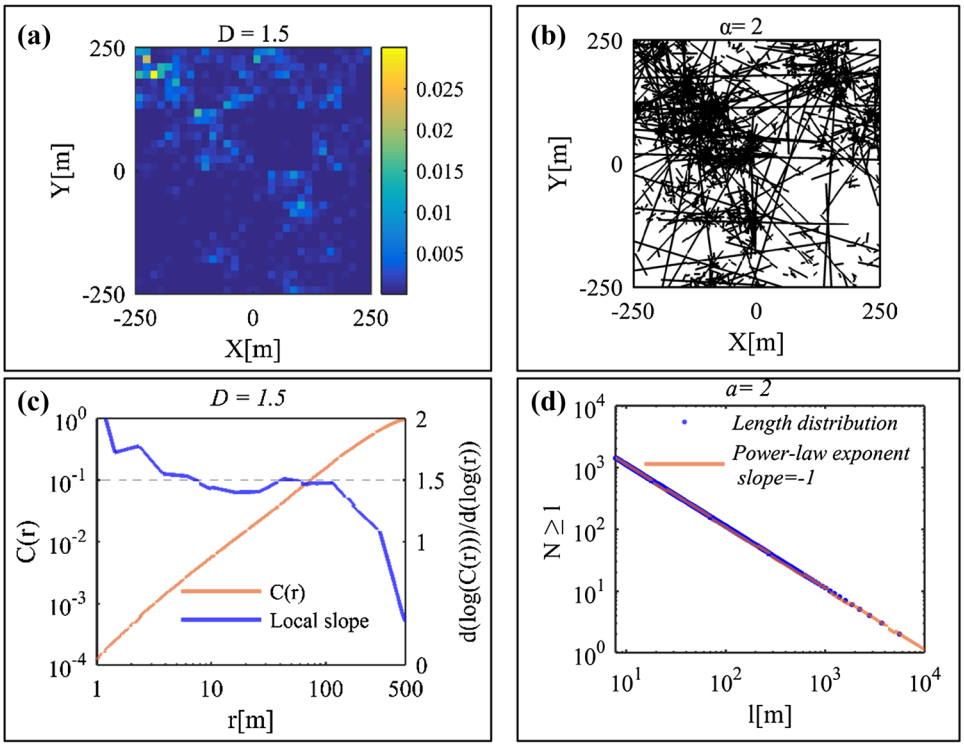

Fig. 2 **a** Realization of a fracture density distribution in a domain of 500 m for a fractal dimension of 1.5 and an l_{min} of 2 m. **b** A DFN realization generated from **a** using a length exponent $a = 2$. The fracture density parameter, α, was taken as 0.3 so as to give approximately 1433 fractures. **c** Correlation function of fracture centers $C(r)$ computed from the density distribution in **a**, together with the local slope and the slope expected for $D = 1.5$. **d** Verification that the cumulative frequency distribution of length computed from **b** is linear with a slope equal to $1 - a$ on a log–log plot

greater number of fractures extending outside the domain and thus have a larger impact on the statistics of the bounded DFN. Figure 3 illustrates the results of applying two different boundary treatment methods to the generation of fractal DFNs with length exponents of $a = 1.5$ and $a = 2.5$ within a domain of length $L = 100$ m. The correlation dimension of fracture centers, D was taken as 1.5 in both cases. In the following, we explore the spatial distribution and length distribution of DFNs, before and after implementing geometric boundary treatments.

2.1.3.1 Removal or Trimming of Fractures that Extend Outside the Domain Figure 4a shows the correlation functions, $C(r)$, and their log–log slope derived from the DFNs shown in Fig. 3a–c for the case $a = 1.5$ that differ in the way fractures that extend outside the domain are treated. The curves denoted 'fractures remain' are for the case where all fractures are counted with their true length, regardless of whether they extend outside the domain boundary shown in red in Fig. 3a. This is presented as a reference. There are 69 fractures that extend outside the domain, which is 17% of the total number of fractures. The curve denoted 'fractures removed' correspond to the case where these 69 fractures are removed (i.e., Fig. 3b). Clearly, removing the fractures completely has a negligible impact on the correlation function, and the log–log slope, neither of which differ significantly from the reference case where all fractures are included. The curve denoted 'fractures trimmed' corresponds to the case where fractures are truncated at the domain boundary. It should be noted that truncating the fractures does not change the total number of fractures. However, it does affect the coordinates of the centers of the trimmed fractures, and hence could affect the statistics of the distance between fracture centers. The log–log slope curve of the trimmed DFN in Fig. 4a lies slightly above the reference curve defined for all fractures, although not greatly so. The cumulative length distributions for the three cases are shown in Fig. 4b. Here, the effect of removing the fractures is to progressively deplete the distribution at all length scales, whereas trimming the fractures limits significant depletion to fractures longer than ~40 m. Figure 4c, d shows the corresponding correlation functions with their log–log slope functions, and the cumulative length distributions for a DFN generated with $a = 2.5$. Again, curves are shown for the cases where fractures that extend outside the domain are either retained with their full length, removed, or trimmed (i.e., Fig. 3 d–f, respectively). For the realization used in this example, 38 fractures extend outside the domain, which is 2% of the total number of fractures. Evidently, the effect of removing or trimming the fractures on the correlation functions and their associated log–log slope functions is negligible in both cases. Comparatively Fig. 4c, d shows that the effect of removing is less considerable when $a > 1.5$. As is the case $a = 1.5$, the cumulative length distribution obtained by trimming was less affected at long fracture lengths than for removing fractures, the deviation from the infinite domain case becoming significant for fracture lengths greater than 40 m.

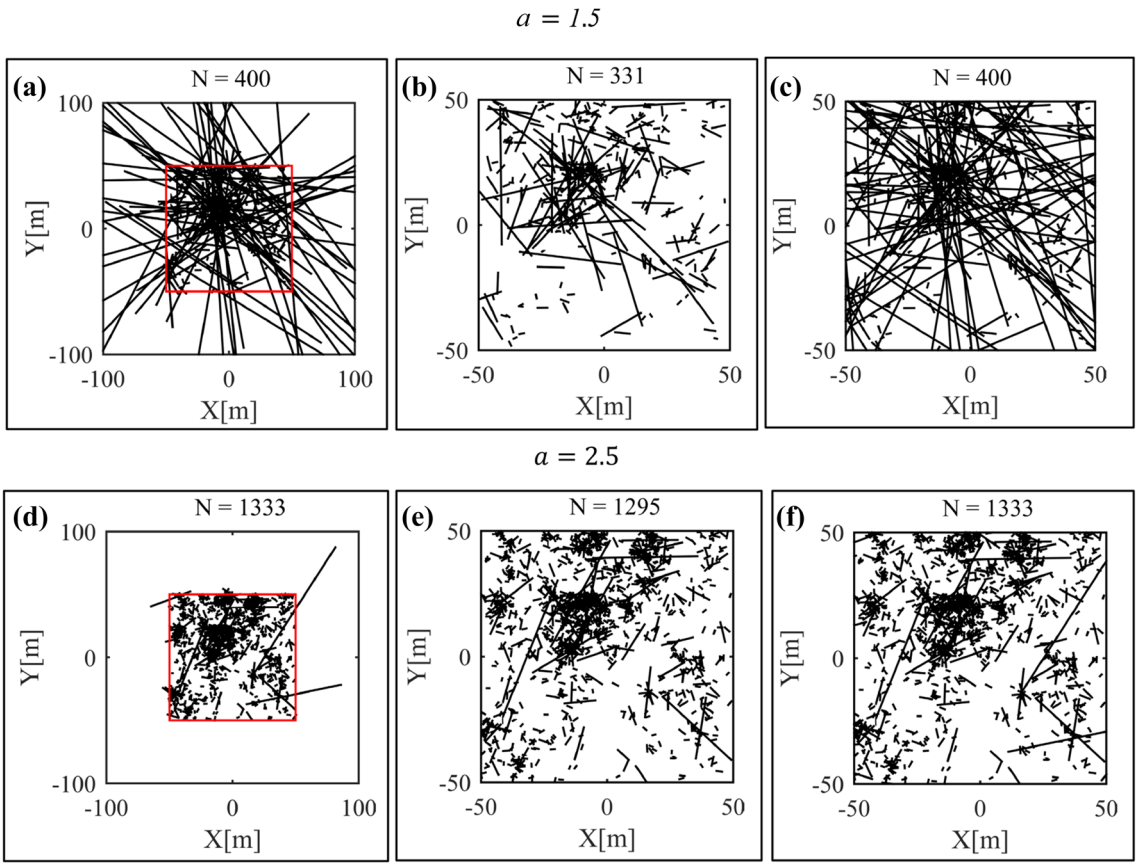

Fig. 3 **a** Realization of a random fractal DFN generated in a domain of length 100 m (outlined in red) with exponents of $a = 1.5$ and $D = 1.5$, and no geometric boundary imposed (i.e., some longer fractures extend outside the frame boundary at ± 100 m). **b** The same DFN generated in **a**, but with all fractures that extend outside the domain removed. **c** The same DFN generated in **a**, but with fractures that extend outside the domain truncated. **d** Realization of a random fractal DFN generated in a domain of length 100 m (outlined in red) with exponents of $a = 2.5$ and $D = 1.5$, and no boundary imposed. **e** The same DFN generated in **d** but with all fractures that extend outside the domain removed. **f** The same DFN generated in **d**, but with fractures that extend outside the domain truncated

3 3D DFN Generation and Stereological Analyses

3.1 3D DFN Generation and Verification

DFN generation in three dimensions is identical to two dimensions, except that the density distribution is slightly different. A 3D probability map of a given fractal dimension is produced by generating eight initial probabilities (instead of four as in 2D fragmentation), subdividing each block into to eight sub-blocks, assigning a random permutation of the eight initial probabilities to the sub-blocks of each parent, and finally multiplying the permuted probabilities by the parent probability. The rest of the generation methodology follows the 2D procedure. Figure 5a represents a 3D DFN generated in a 500 m domain using the dual power-law model with the parameters $D = 2.7$, $a = 2.8$, $\alpha = 0.02$ and $l_{\min} = 10$ m. Figure 5b, c demonstrates the fractal nature of the spatial and length distributions of the fracture network respectively (r and R represents the distance between fracture centers and the radius of a fracture plane). For this demonstration, fractures that extend outside the domain boundary were included with their full length.

3.2 Stereological Analysis

Stereological relationships relate the geometrical properties of a DFN in different dimensions (e.g., a 2D trace plane intersecting 3D network or a 1D scanline intersecting a 2D trace plane). A detailed stereological analysis of fractal DFNs has been presented by Darcel et al. (2003b). In this section, we focus on the relationships derived for relating 1D scanlines intersecting 2D and 3D synthetic networks.

For the length distributions, there is a simple relationship between $a_{2D}$and a_{1D} given by Eq. (14).

$$a_{1D} = a_{2D} - 1 \tag{14}$$

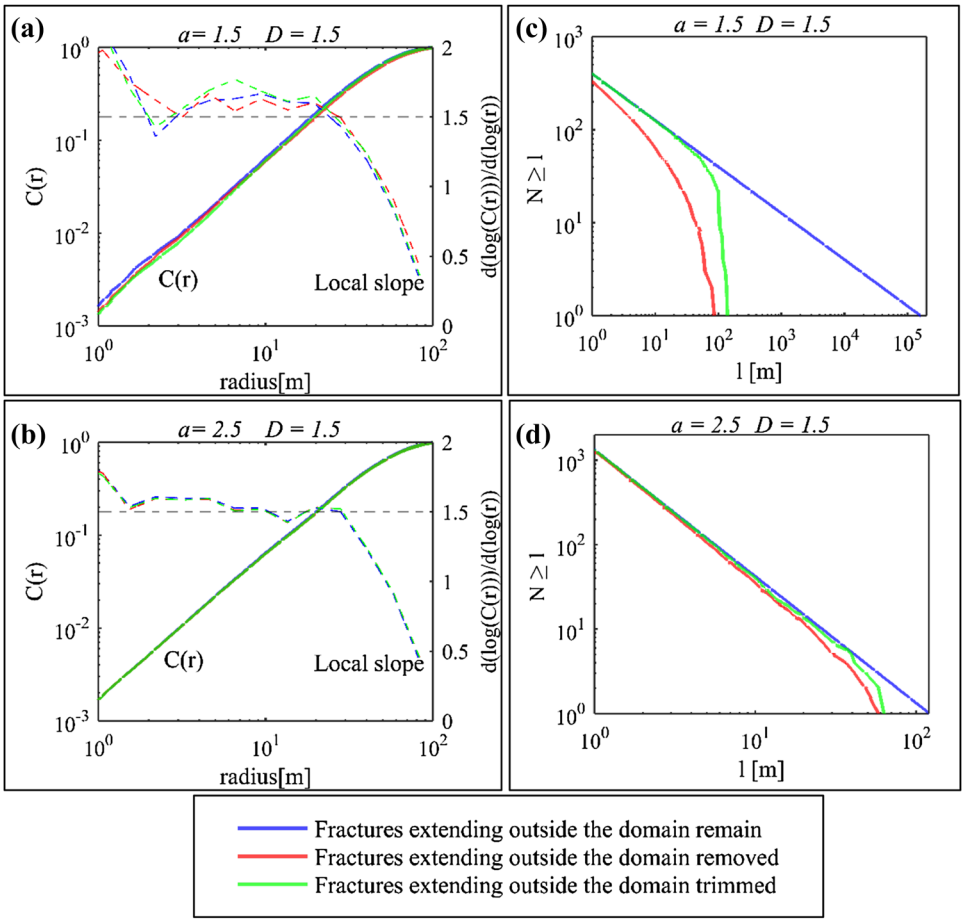

Fig. 4 Effect on correlation functions and length distributions of applying two different approaches to the problem of fractures that extend beyond the domain boundary, namely to remove the fractures (blue), or to trim them so they do not extend beyond the domain boundary (green). The curves obtained by including such fractures with their true length are shown for comparison (brown), **a** correlation functions and their log–log slope, and **b** length distributions derived from the DFNs in Fig. 3a, b which correspond to the case $a = 1.5$. The domain length is 100 m. The log–log slopes of the $C(r)$ functions should be flat and equal to 1.5 (i.e., a correlation dimension of 1.5), as shown by the black dashed line. **c** Correlation functions and their log–log slopes and **d** length distributions derived from the DFNs in Fig. 3d, e which correspond to the case $a = 2.5$

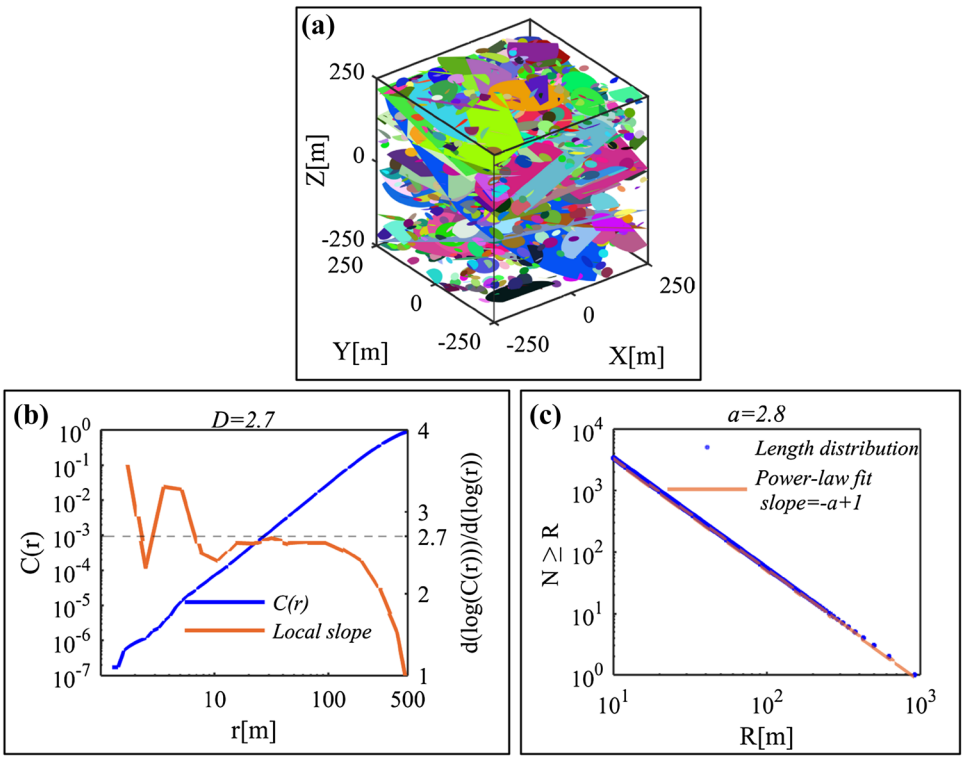

Fig. 5 **a** A synthetic 3D network generated in a 500 m domain using dual power-law model with $D = 2.7$, $a = 2.8$, $l_{min} = 10$ m and $\alpha = 0.02$. **b** Correlation function and its local slope of the generated network. **c** Complementary cumulative length distribution of the generated network (N is the number of fractures larger than size of R)

Since the lengths of fractures intersecting a borehole are essentially not observable, this relationship is not relevant here. The exponent of the spatial distribution of fracture centers (D_{2D}) in a 2D $L \times L$ domain is related to the exponent of the spatial distribution of fracture intersections of a 1D scanline of length L (D_{1D}) by a relation whose form depends on the length exponent of the DFN, as given in Eqs. (15)–(17) after Darcel et al. (2003b):

$$D_{1D} = 1, \quad a_{2D} \leqslant 2 \text{ and } a_{2D} \leqslant D_{2D} \tag{15}$$

$$D_{1D} = D_{2D} - a_{2D} + 1, \quad a_{2D} \leqslant 2 \text{ and } a_{2D} \geqslant D_{2D} \tag{16}$$

$$D_{1D} = D_{2D} - 1, \quad a_{2D} \geqslant 2 \tag{17}$$

Darcel et al. (2003b) performed numerical simulations with synthetic DFNs to attempt to verify the above stereological relationships but found that they were only partly valid. Here we use a different stereological analysis approach to clarify the range of validity of Eqs. (15)–(17).

The procedure used for the 2D stereological analysis is as follows. Fractal fracture networks were generated in a domain of 512 m × 512 m. The length exponent was assumed to lie between 1.3 and 3.5 and the correlation dimension of fracture centers was varied between 1 and 2. The minimum length of the fractures in each model was set to 1 m. Fractures that extended beyond the boundaries were trimmed. For each fracture network generated with a given D_{2D} and length exponent, scanlines were placed every 1 m parallel to both x- and y-axis (i.e., 1025 scanlines in total) and the locations of fracture intersection points along each scanline determined. The correlation functions of these fracture intersection points along each scanline yielded estimates of D_{1D} within the range of 1–100 m. The resulting estimates of D_{1D} were then plotted as a function of the correlation dimension, D_{2D}, of the fracture network in question.

The analysis was performed on two sets of 2D fractal DFNs with different length exponents of $a_{2D} = 1.5$ and $a_{2D} = 2.5$. For each length exponent, the correlation dimension D_{2D} was varied from 1.1 to 1.9 in steps of 0.1 (i.e., D_{2D} =1.1, 1.2,…, 1.9), and a single DFN with random fracture orientation generated for each step. For each value of length exponent a_{2D}, the constant α in Eq. (1) was adjusted for each step to produce a large and constant number of fractures centered in the domain, thereby eliminating the effects of the number of fractures on the analysis whilst ensuring a large number of intersections with 1D sampling lines. For $a_{2D} = 1.5$, α was chosen so as to produce approximately 20,000 fractures (approximate P_{21} of 40), whilst a value that generated approximately 200,000 (approximate P_{21} of 4) was used for $a_{2D} = 2.5$. The difference in the number of fractures compensates for the tendency for $a_{2D} = 2.5$ to generate proportionally fewer larger fractures and hence fewer intersections. Figure 6a shows the resulting values of D_{1D} obtained as a function of D_{2D} for $a_{2D} = 1.5$ together with the trends expected from Eqs. (15) and (16). Clearly, for $D_{2D} \geqslant a_{2D}$ =1.5, the values of D_{1D} scatter closely around 1, which is consistent with expectations from Eq. (15). However, for $D_{2D} \leqslant a_{2D}$, the analysis indicates a progressive discrepancy between the values of D_{1D} obtained from the realizations and the stereological relationship of Eq. (16). Similar observations are reported by Darcel et al. (2003b) who referred to this range as a transition regime.

The corresponding results for a length exponent of 2.5 are shown in Fig. 6b together with the expected trend from Eq. (17). It is evident that the D_{1D} values derived from the scan lines overestimate the values expected from Eq. (17) for all values ofD_{2D}, the overestimate increasing for smaller values of D_{2D}. Similar results were found by Darcel et al. (2003b) who plotted only the average values of the D_{1D} values as a function of D_{2D}.

The stereological analyses presented above consider DFNs that have a random orientation of fractures. However, fractures mapped in boreholes or outcrops commonly fall into one of several discrete orientation sets that reflect the fracture families present in the rock mass. As an example, Ziegler et al. (2015) used a fracture imaging log run in the Basel-1 borehole to characterize the natural fracture distribution in the rock mass penetrated by the well. They identified six potential fracture sets based on their orientation. To investigate the impact of preferred orientation of fractures on the stereological analysis, 2D fractal DFNs were generated that contained only two fracture sets which subtended angles of 45° and 135° from the x-axis. The procedure and parameter values used in the stereological analyses were the same as those applied for the random fracture orientation cases. The results, shown in Fig. 7c, d for $a_{2D} = 1.5$ and $a_{2D} = 2.5$ respectively, are in close agreement with the random orientation cases. Various fracture orientation configurations have been tested leading to the same conclusion.

It is of practical interest to examine the stereological relationship between fractures sampled along 1D scanlines (i.e., boreholes) cutting through 3D fracture networks. Darcel et al. (2003b) have shown the equations defining the theoretical stereological relationships between 2D trace planes and 3D synthetic networks are given by Eqs. (18–20).

$$D_{2D} = 2, \quad a_{3D} \leqslant 2 \quad \text{and } a_{3D} \leqslant D_{3D} - 1 \tag{18}$$

$$D_{2D} = D_{3D} - a_{3D} + 1, \quad a_{3D} \leqslant 2 \text{ and } a_{3D} \geqslant D_{3D} - 1 \tag{19}$$

$$D_{2D} = D_{3D} - 1, \quad a_{3D} \geqslant 2 \tag{20}$$

Combining the above 3D to 2D equations with the 2D to 1D relations for the majority of natural fractured

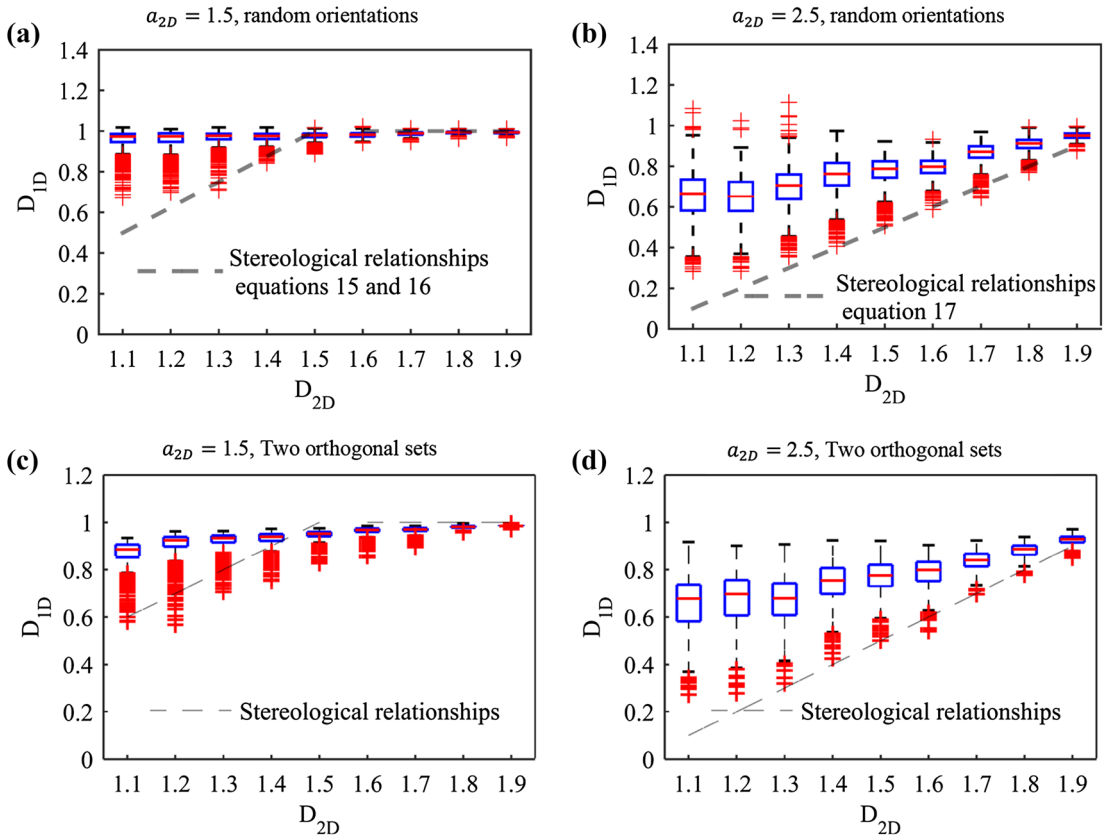

Fig. 6 Stereology plot of 1D lines sampling a 2D fractal fracture network. **a** Values of D_{1D} obtained from DFN realizations with random fracture orientations generated with $a_{2D}=1.5$ as a function of D_{2D}. For a given D_{2D} value, the red line in the box denotes the median value of D_{1D} taken over the realizations, and the lower and upper edges of the box denote the 25 and 75 percentile values, respectively, whose difference denotes the inter quartile range (IQR). The horizontal short black lines lie 1.5*IQRs* from the upper and lower edges of the 25 and 75 percentiles. Red crosses are realization falling outside this range. **b** Same as **a** but with $a_{2D} = 2.5$ with random fracture orientations. **c** Same as **a** but with $a_{2D} = 1.5$ and two orthogonal sets. **d** Same as **a** but with $a_{2D} = 2.5$ and two orthogonal sets

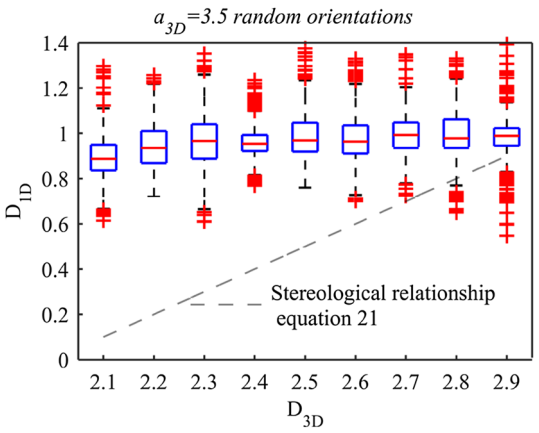

Fig. 7 Stereology plot of 1D lines sampling a 3D fractal fracture network. Values of D_{1D} obtained from DFN realizations with random fracture orientations generated with a length exponent $a_{3D} = 3.5$ as a function of D_{3D} with random orientations

systems (i.e., $a_{3D} \geqslant 3$ and $a_{2D} \geqslant 2$) gives the required 3D to 1D equation as Eq. (21).

$$D_{1D} = D_{3D} - 2, \quad a_{3D} \geqslant 3 \tag{21}$$

We performed a similar stereological analysis to those done previously, this time using 3D DFNs generated with $a_{3D} = 3.5$, and D_{3D} varied from 2.1 to 2.9 in steps of 0.1. Fracture orientations were random. For each DFN generated for each step, the 1D correlation dimension, D_{1D}, was measured along 512 scanlines aligned with the z-axis and spaced every meter in the x-axis direction. The resulting D_{1D} values are shown as a function of D_{3D} in Fig. 7 for $a_{3D} = 3.5$, together with the trend from Eq. (21). For all values of a_{3D}, the computed D_{1D} remains on average close to 1. This illustrates that it is impossible to estimate the correlation dimension of a 3D fractal fracture network from 1D line samples taken from boreholes through it.

4 Techniques of Estimating Fractal Dimension Applied to Synthetic 1D Fractal Fracture Distributions

Fractal geometry has been widely applied to characterize fracture intersections along 1D scanlines in natural fracture systems (e.g., Boadu and Long 1994; Ledésert et al. 1993; Manning 1994; Merceron and Velde 1991; Moein et al. 2016; Roy et al. 2014). Here, we review the available techniques to estimate the fractal dimension of fractures intersecting 1D scanlines. Then, we apply these techniques to estimate the fractal dimension of synthetic patterns of known fractal dimension to determine the best and most reliable methodology to characterize 1D fracture patterns.

4.1 Synthetic 1D Fracture Network Generation

We applied the Multiplicative Cascade process to generate 1D fractal patterns (i.e., points along a scanline) of given fractal dimension using a procedure which is broadly similar to that described previously. The main differences are: (1) the generation domain is reduced to a line of size L *m* (instead of a square of $L \times L$ m^2) and the number of initial probabilities is reduced to 2 (instead of four). The fragmentation process is accomplished by dividing the domain size into two sub-domains in each iteration (i.e., $l_{ratio} = 2$). The initial parameters required to generate fractal patterns of fracture intersection points on a single scanline are the number of iterations n, the number of fracture intersection points N_t, and the scanline length of L. For our application, since we are only interested in the spatial distribution of intersection points, we skip the steps that assign fracture length to fracture locations on scanlines. Here, we set $L = 512$ m, $n = 16$ and populate 1000 random fracture locations with a fractal dimension of $D_{1D} = 0.75$. Figure 8a shows a schematic representation of fractures on a sample synthetic scanline with an original length of 512 m. For the sake of clarity, only 64 m of the scanline is presented in this figure. In the following, we apply three different techniques to estimate the fractal dimension of this synthetic 1D scanline and evaluate the limitation and accuracy of each methodology.

4.2 Fractal Dimension Estimation

4.2.1 Two-Point Correlation Function

The two-point correlation function computes the correlation dimension similar to 2D networks using Eq. (2). Figure 8b displays the application of two-point correlation function to compute the correlation dimension (D) of the synthetic fracture intersection point patterns of Fig. 8a. The computed correlation dimension is reasonably stable and close to the initial fractal dimension ($D = 0.75$) over almost two orders of magnitude.

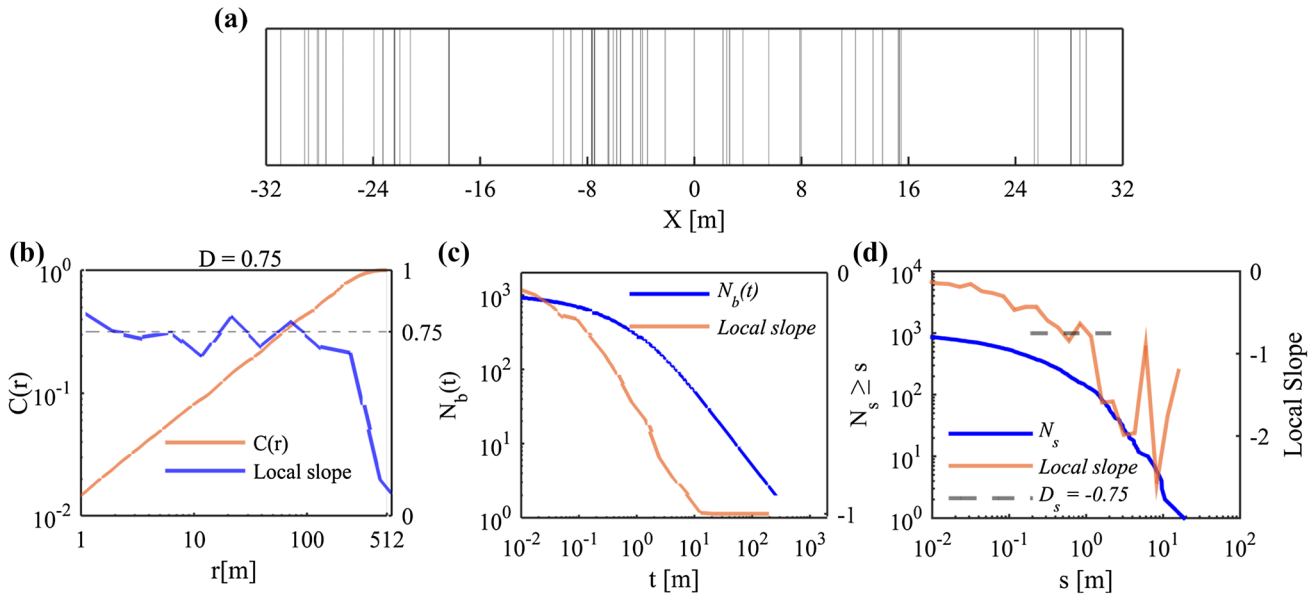

Fig. 8 **a** A schematic view of a synthetic fracture pattern on a 1D scanline domain, generated using a 1D Multiplicative Cascade process with a $D_{1D} = 0.75$, $L = 512$ m, and $n = 16$. For the sake of clarity, only 64 m of the scanline is plotted. The number of fractures in the entire domain is 1000. **b** Log–log plot of the two-point correlation function and its local slope of the scanline shown in **a**. **c** Box-counting analysis and its corresponding local slope of the synthetic 1D scanline generated in **a**. **d**Complementary cumulative distribution of spacing and local slope of the synthetic 1D scanline generated in **a**

4.2.2 Box-Counting Technique

The box counting technique consists of covering the data space (here the scanline) with rulers of equal sizes t laid end-to-end and determining how many of the rulers contain data $N_b(t)$. The initial ruler length is chosen as the scanline length, and the procedure repeated sequentially using progressively smaller rulers that are fractions of the scanline length. If the distribution of fracture intersections follows a fractal behavior, then $N_b(t)$ should be related to the rule length t by the relation $N_b(t) \sim t^{-D_b}$ (Chilès 1988; La Pointe 1988). Thus the box-dimension, D_b, can be evaluated by measuring the local slope of $N_b(t)$ vs. t in a log–log plot. Note that some authors plotlog $\left(\frac{N_b(t)}{N}\right)$ vs. log(t), although in that case the slope will be equal to $1 - D_b$ (e.g., Ledésert et al. 1993; Velde et al. 1990). In general, this slope will not be constant over the entire range of t, as can be appreciated by considering the behavior at extreme values. When there is a small number of large rulers, all rulers will contain data and the local slope will essentially be -1. On the other hand, when rulers are shorter than the minimum data spacing, the number of rulers containing data will become a constant equal to the number of data points and the slope on the log–log plot will tend to zero. In between these two extreme cases, a regime with a constant slope should develop if the data set is truly fractal, and this constant slope is an estimator of the fractal dimension of the data set. Figure 8c shows the application of the box-counting techniques to compute the box-dimension of the dataset in Fig. 8a. Evidently, the plot of log($N_b(t)$) versus log(t) does not show a fractal regime in which the local slope is constant for a considerable range.

4.2.3 Power-Law Distribution of Spacing

This method considers the spacing of fracture intersection points along a scanline or borehole. An approach to estimating the fractal dimension of the fractal intersection points is to compute the cumulative spacing distribution (Gillespie et al. 1993). That is, to plot the logarithm of the number of spacings N_s greater than or equal to a specific spacing (s) versus the logarithms of the specific spacing. If the distribution is fractal over a limited range, then the relation, $N_s(s) \sim s^{-D_s}$ should be valid, and the slope should yield the fractal dimension, D_s. Although estimating the power-law scaling exponent from cumulative density distribution may be biased (Bonnet et al. 2001), we aim to evaluate the stationarity of the scaling exponents compared to other techniques (i.e., extracting the exact scaling exponent is not the main purpose). Figure 8d displays cumulative distribution of fracture spacing derived from synthetic patterns on Fig. 8a. As was found for the box-counting technique, there is no extensive range over which the local slope of $N_s(s)$ has a constant value. A short plateau can be seen between $s = 50$ cm and 1 m, at a slope and hence D_s value of 0.75, denoted by the dashed line in Fig. 8d. However, the feature is insufficiently distinct to be considered a priori as a reliable indicator of fractal behavior.

The results of applying the three techniques to estimate the fractal dimension of the 1D fracture spacing dataset show that the correlation function delivers a clear and stable estimate that is in accord with the fractal dimension used in generating the dataset. Although the power-law distribution of fracture spacing yields a similar fractal dimension, the slope plateau is not clearly recognizable as such in the log–log plot, and has a smaller range of validity. The estimate of fractal dimension from the box-counting technique is biased and shows no constant slope over any range. Bour et al. (2002) applied the classical box-counting technique directly to the 2D outcrops from Hornelen basin and found no evidence of fractal behavior. In contrast, the two-point correlation function between fracture centers indicated fractal behavior over a wide range of length scales and yielded an estimate of the correlation dimension of the fracture centers which appears to be the true fractal dimension.

5 Scaling of 1D Natural Fracture Distribution in Three Deep Boreholes

The primary source of information on natural fracture networks in deep reservoirs stems from borehole wall image logs such as the acoustic televiewer. Fractures can be identified and their orientation obtained by fitting sinusoids to their traces on unwrapped images. Although the resolution of acoustic televiewer logs does not permit the identification of very thin discontinuities (Genter et al. 2010), the resulting fracturing dataset usually provides a reasonably complete sampling of the fracture families present in a rock mass. The fracture datasets discussed here were derived from a 5 km deep geothermal well, Basel-1, located near Basel in Switzerland, and two 5 km deep wells, GPK3 and GPK4, at the Soultz Geothermal Project at Soultz-sous-Forêts in France. Both sites are located in the Upper Rhine Graben, a Cenozoic rift system (Dèzes et al. 2004). At both sites, the boreholes penetrate a Cenozoic and Mesozoic sedimentary series and reach the basement at 2.5 km in Basel and 1.4 km in Soultz-sous-Forêts. In Basel, the basement is essentially composed of a monzogranite (Häring et al. 2008). The top section of the basement was exposed at the surface prior the deposition of the Mesozoic sediments and thus is altered. In Soultz, the basement is mostly composed of a porphyric monzogranite with various level of hydrothermal alteration while the deepest part of the well penetrates a two-mica granite (Dezayes et al. 2010). Figure 9 shows stereographic

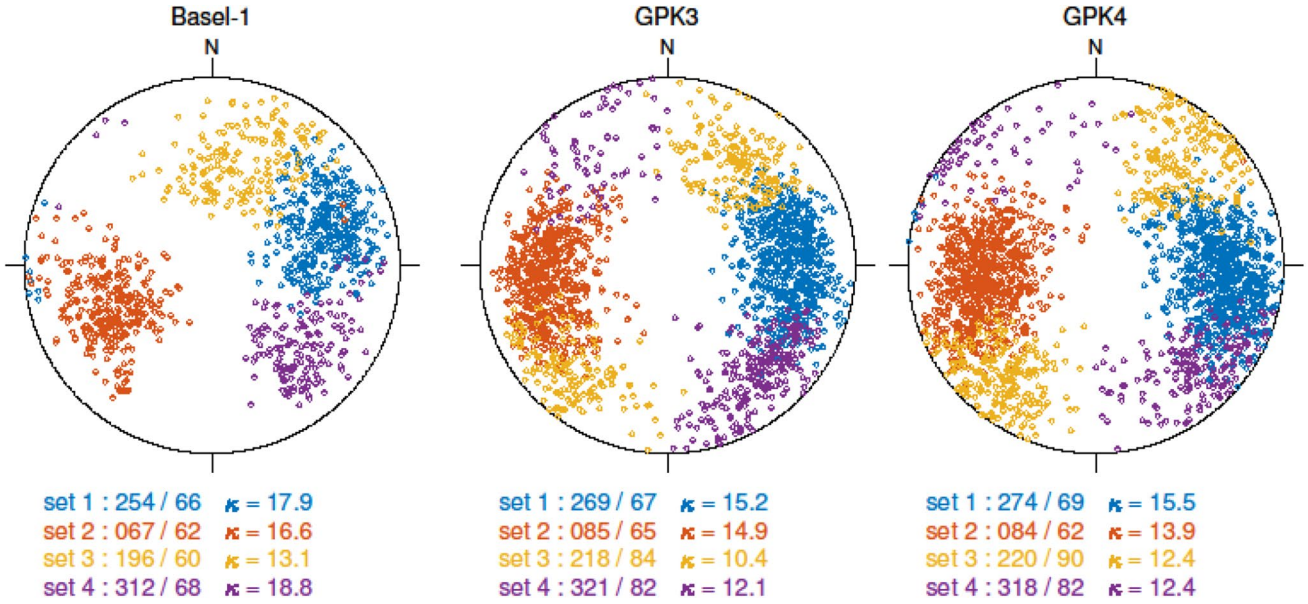

Fig. 9 The stereonet (lower hemisphere, equal area projection) plots of the poles of natural fractures in Basel-1, GPK3 and GPK4 with corresponding Fischer coefficients of each set

Table 1 Number of fractures in sets and corresponding mean orientations in Basel-1 (Ziegler et al. 2015)

Fracture set	Number of fractures	Mean dip direction (°)	Mean dip angle (°)
1	348	250	66
2	297	68	62
3	173	195	61
4	152	307	68
5	53	37	68
6	12	133	76

Total number of fractures = 1164

projections of the orientation of fractures derived from log runs in these three boreholes. The depth of fractures in the borehole logs has been converted from measured depth (MD) to true vertical depth (TVD) below ground. Several analyses were run using both MD and TVD and the same results were obtained. In earlier studies, the fractures in each borehole were picked and assigned to fracture sets based on their orientation. The sets and their mean orientations are listed in Tables 1 and 2, and are ranked in terms of the number of fractures they contain. Six fracture sets were recognized in Basel-1 (Ziegler et al. 2015) and seven sets in GPK3 and GPK4 (Valley and Genter 2007; Ziegler et al.

Table 2 Number of fractures in recognized sets and corresponding mean orientations in boreholes GPK3 and GPK4 at the Soultz-sous-Forêts site

Fracture set	Number of fractures		Mean dip direction (°)		Mean dip angle (°)	
	GPK3	GPK4	GPK3	GPK4	GPK3	GPK4
1	625	749	269	272	68	70
2	584	708	85	85	66	64
3	324	411	136	122	72	74
4	297	231	280	271	74	77
5	27	40	177	200	33	24
6	63	55	185	203	76	80
7	6	21	189	170	54	46

Total number of fractures in GPK3 = 1926

Total number of fractures in GPK4 = 2115

2015), although some fractures could not be assigned to any of the fracture sets.

5.1 Comparison of the Scaling Properties of 1D Fracture Distributions Obtained Using Different Techniques

Here, we applied the two-point correlation function technique, the box-counting method and statistical power-law distribution of spacing to compute the fractal dimension of fracture patterns in Basel-1 well. For this analysis, the entire fracture dataset is used without regard to the different sets (i.e., orientations). Figure 10a shows that the fractal dimension given by the correlation dimension derived from the two-point correlation method is reasonably constant over two orders of magnitude. On the other hand, the box-counting technique does not show a plateau in the entire range (Fig. 10b) and the power-law analysis of spacing distribution shows a constant slope for less than one order of magnitude with a fractal dimension of 0.21 (Fig. 10c). According to the analysis of synthetic data (Sect. 3.1), the correlation dimension seems to be the true fractal dimension of fracture patterns in deep boreholes.

5.2 Fractal Dimension Estimation of 1D Spacing Distributions of Fractures in Different Sets

In this study, we consider only the first four sets (1–4) of the three boreholes which are the most populous. The number of fractures in other sets is too small to perform a fractal analysis. No consideration was given to the confidence of the identification of the individual fractures. For each of the four sets, two-point correlation functions of fracture intersection depths (in TVD) along the boreholes were computed for 500 points logarithmically distributed uniformly in the range 0.1–10,000 m (i.e., 100 for every order of magnitude). The local slopes of the log–log plots of the $C(r)$ function were calculated for 25-point wide windows that were progressively moved across the $C(r)$ curves without overlap, thereby giving four slope values per decade.

The $C(r)$ and log–log slope functions obtained from the analysis of the Basel-1 fracture sets are shown as functions of r in Fig. 11. In all cases, the log–log slope appears reasonably flat save for local fluctuations for a range of r values that span at least 2–200 m, demonstrating that the spacing of the fracture intersection points is fractal over scales of at least 2–200 m. The best-fitting horizontal lines to the slope functions over this range gave the D_{1D} estimates of between 0.65 and 0.75, which are listed in Table 3 together with their standard deviations and corresponding ranges of validity.

Identical analyses were performed on the natural fracture sets imaged in GPK3 and GPK4 of the Soultz-sous-Forêts geothermal reservoir, and the correlation and log–log slope functions are shown in Figs. 12 and 13 respectively. In all cases, the log–log slope has a reasonably constant value over two and in some cases, three orders of magnitude (Table 3). The correlation dimension (D_{1D}) estimates for GPK3, obtained from the best-fit horizontal line over range 1–200 m, vary between 0.71

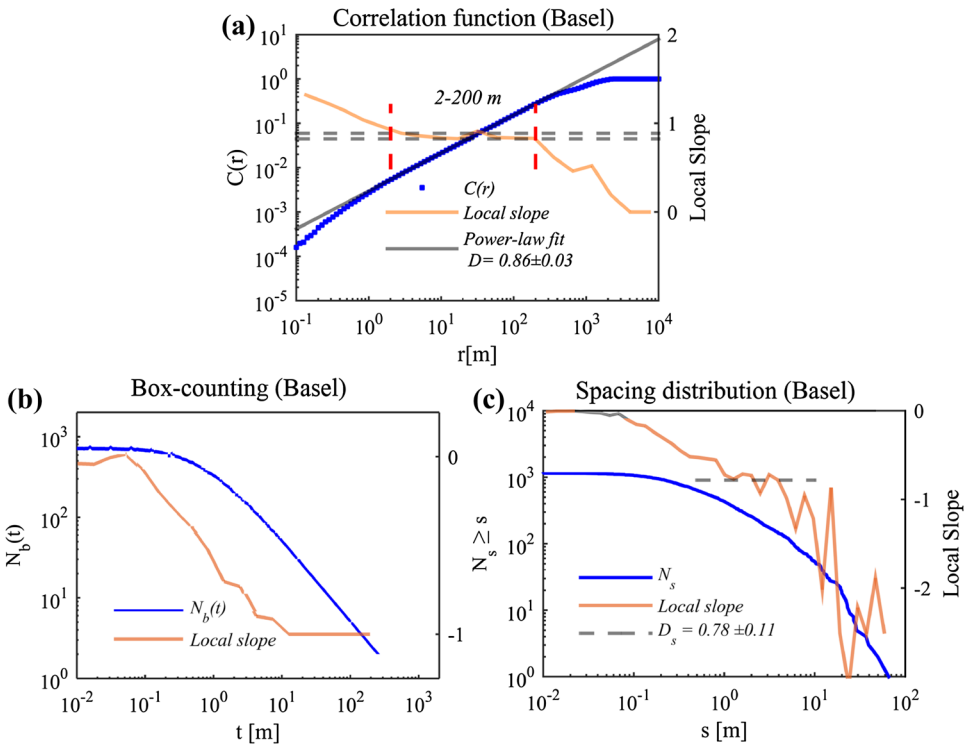

Fig. 10 Application of three different techniques to compute the fractal dimension of fracture patterns in Basel-1 borehole, **a** two-point correlation function, **b** box-counting technique and **c** statistical distribution of spacing

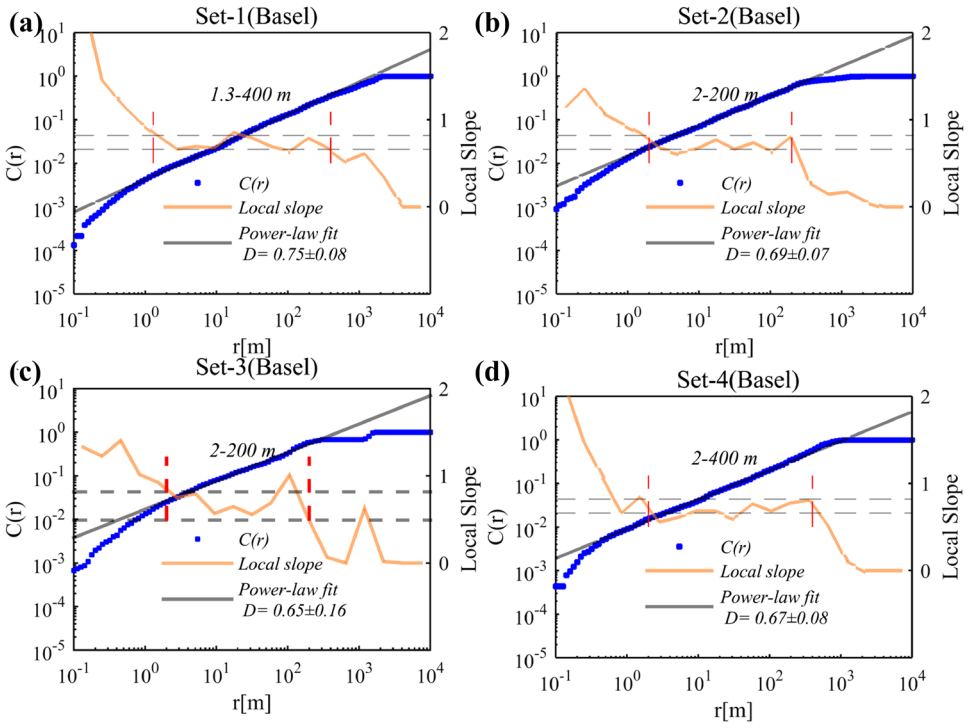

Fig. 11 Correlation and log–log slope functions of fracture sets in the Basel-1 well. The best-fit horizontal line to the log–log slope function over the *r* range of 2–200 m which gives the value of D_{1D} is shown together with the standard deviation. The range of r over which fractal scaling is seen is indicated between the vertical lines drawn at the 1 sigma variation of D_{1D}. **a** Set 1, **b** set 2, **c** set 3, **d** set 4

Table 3 1D Fractal dimension of fracture patterns in three deep boreholes and the corresponding range

Fracture set	D_{1D} (Basel-1) Range	D_{1D} (GPK3) Range	D_{1D} (GPK4) Range
1	0.75 ± 0.08 1.3–400 m	0.74 ± 0.05 2–1000 m	0.75 ± 0.11 1–2000 m
2	0.69 ± 0.07 2–200 m	0.72 ± 0.05 3–1000 m	0.74 ± 0.1 2–2000 m
3	0.65 ± 0.16 2–200 m	0.71 ± 0.08 2–1000 m	0.68 ± 0.12 1–1000 m
4	0.67 ± 0.08 2–400 m	0.72 ± 0.09 06–200 m	0.66 ± 0.09 1–200 m
Entire dataset	0.86 ± 0.03 2–200 m	0.88 ± 0.02 2–1000 m	0.87 ± 0.06 2–1000 m

Correlation dimension obtained from the analyses of fracture intersection spacing in the three wells

and 0.75 (Table 3), whereas those for GPK4 range between 0.66 and 0.75.

5.3 Fractal Dimension Estimation of 1D Spacing Distributions of all Fractures in Each Borehole

The correlation and slope functions of all fractures in the Basel-1, GPK3 and GPK4 datasets are shown in Fig. 14a–c, respectively. No consideration is given to the orientation of the fractures. For Basel-1, the log–log slope shows a constant value over two orders of magnitude, and for GPK3 and GPK4, over three orders of magnitude (Table 3). The estimated fractal dimensions for the three holes are very close to each other, being 0.86, 0.88 and 0.87 for Basel-1, GPK3 and GPK4 respectively, and the associated standard deviation of the local slope within the fractal range which spans 2–500 m is less than 0.06 in all cases.

6 Discussion

The generation of discrete fracture network models conditioned by available observations from boreholes or outcrops is required in practically all subsurface rock mass characterization programs (e.g., Watanabe and Takahashi 1993). The approach investigated here makes the assumption that fracture networks can be considered as fractal objects. Fractal fracture networks require the values of scaling parameters that control the position and length of the fractures that form the network to be specified. The dual power-law mathematical model proposed by Davy et al. (1990) is a convenient way of describing the fracture network. The model contains two scaling parameters: the correlation dimension *D*, which controls the position of fracture centers, and the length exponent *a*, which controls the fracture length distribution. One-dimensional, two-dimensional and three-dimensional synthetic fracture datasets honoring this model can be generated using the Multiplicative Cascade process. This model forms the basis for our analyses.

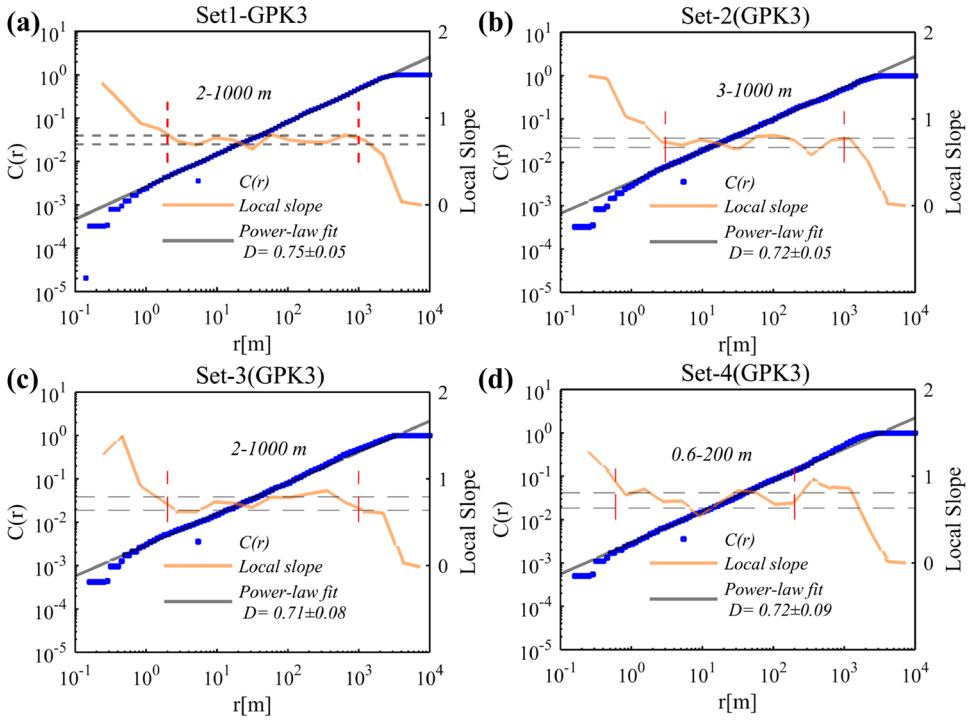

Fig. 12 Correlation and log–log slope functions in log–log space for the four fracture sets identified in the GPK3 well at the Soultz geothermal site: **a** set 1, **b** set 2, **c** set 3, **d** set 4

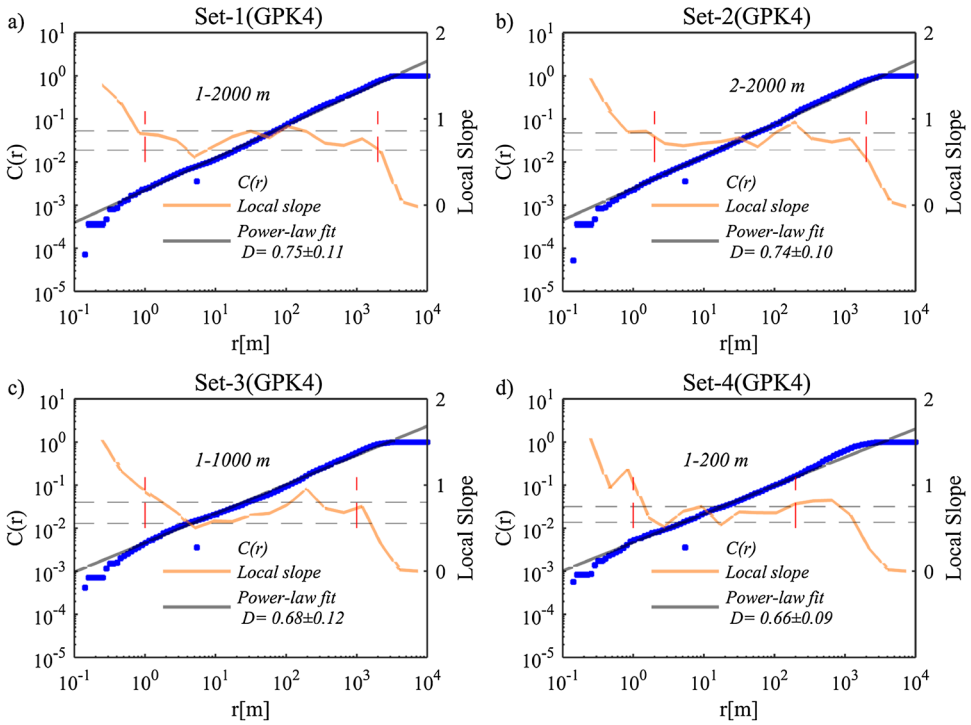

Fig. 13 Correlation and log–log slope functions local slopes for the four fracture sets identified in the GPK4 well at the Soultz geothermal site: **a** set 1, **b** set 2, **c** set 3, **d** set 4

The Levy–Lee flight process as implemented in the Fracman software package was also considered as a fractal fracture network generator. However, the fractal dimension of fracture centers of the generated network was found to differ from the input value, a result what is believed to be due to the effects of the finite size of the domain (Darcel 2002). Experiments with fracture networks generated in finite domains with the multiplicative cascade process showed that removal or trimming of fractures that crossed the domain boundary did not significantly impact the correlation (i.e., fractal) dimension of fracture centers of the network. However, only trimming preserved the fractal nature

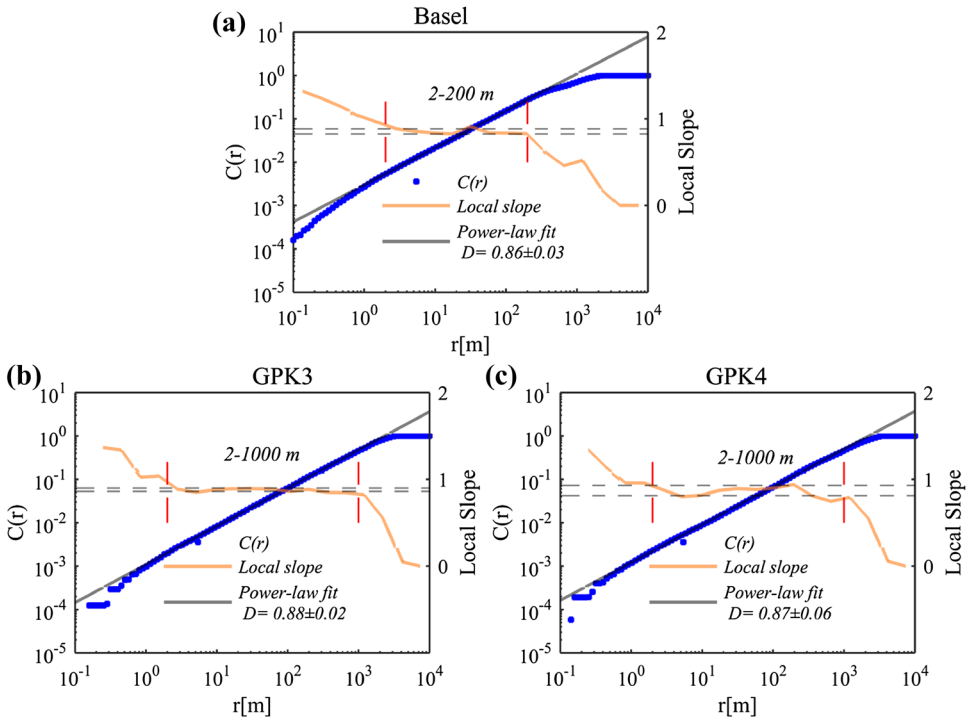

Fig. 14 Correlation and log–log slope functions derived from all fractures (grouped into one dataset regardless of their orientation) intersecting **a** the Basel-1 well, **b** the GPK3 well, **c** the GPK4 well

of the fracture length distribution, the deviation from fractal behavior becoming significant for larger fractures within the domain.

The scaling inherent in fractal fracture networks is quantified by scaling exponents (i.e., fractal dimensions). For 2D and 3D fracture networks, the fractal dimensions obtained from applying different measurement methods represent the scaling properties of different attributes of the fracture networks. For example, box-dimension is a measure of the space filling characteristics of the fractures (which inherently accounts for the length and center-to-center separation of the fractures) and correlation dimension reveals the clustering of fracture centers. Bour et al. (2002) applied the box-counting technique to a fracture exposure in the Hornelen Basin, Norway and noted fractal behavior over a limited range of scales, whereas the two-point correlation function method indicated fractal behavior over a much larger range of scales. In contrast to 2D and 3D fracture networks, the distribution of fractures along 1D scanlines or boreholes depends only on the separation of fracture intersection points (i.e., the fracture length does not play any role in computing the scaling exponent). For this simple case of points along a line, it might be assumed that if the distribution is indeed fractal, then the same fractal dimension would be obtained regardless of the technique used to estimate it. However, our experiments with synthetic 1D fracture spacing data of known fractal dimension showed that the two-point correlation method was the only technique that yielded stable and correct estimates for the fractal dimension of the series, as given by the correlation dimension. The box-counting technique and power-law distribution of spacing methods did not deliver reliable estimates of the fractal dimension.

The computation of 1D correlation dimensions for fracture datasets from one deep borehole in Basel, Switzerland (Basel-1) and two deep boreholes in Soultz-sous-Forêts, France (GPK3 and GPK4) led to very similar values ranging from 0.86 to 0.88 when considering all fracture orientations together. This fractal scaling is seen to be valid over more than two orders of magnitudes (i.e., typically in the range 2–1000 m), which covers the entire range that one can reasonably expect to resolve from the data lengths in question (2.5 km for Basel-1 and 3.5 km for GPK3 and 4) before finite size effects become manifest. This constitutes strong evidence that the fracture networks investigated follow a fractal organization. Performing the analyses for each borehole on sets of fractures of similar orientations, yields correlation dimensions that are slightly lower, the values ranging from 0.65 to 0.75, although the ranges of validity of fractal scaling still span more than two orders of magnitude.

The data from the boreholes GPK3 and GPK4 at the Soultz site are of particular interest since they are only 30 m apart in the upper kilometer of the granite section and hence they sample essentially the same rock mass. The inter-well distance increases up to 700 m toward the bottom of the holes. Thus, the constancy in correlation dimension estimates with depth and laterally in these boreholes indicates vertical and lateral homogeneity of the fractal characteristics of the fracture network in the rock volume sampled by the wells.

The physical interpretation of the correlation dimension D_{1D} in terms of the organization of the fracture network is not trivial (Davy et al. 2010). Uniformly spaced fractures or uniform randomly distributed fractures (Poisson's process) will have a correlation dimension of 1.0. Smaller values of D_{1D} will imply some clustering of the fractures. Our values for D_{1D} suggest some clustering of the fractures, but not strong clustering. Previously reported scaling exponents of data from EPS1 at Soultz-sous-Forêts reported values in the range of 0.2–0.4 corresponding to the box-dimensions of 0.6–0.8 (Ledésert et al. 1993), which are very close to the ranges of our fractal dimensions. The fractal dimension values obtained by fitting a power-law to the cumulative spacing distribution for various fracture sets in GPK3 and GPK4 yielded values of 0.63–1.0. These values are also similar to our findings, although the stability of the local slopes was not satisfying (Valley 2007). The degree of clustering and the fractal dimension is also interpreted by some authors as an indication of the "saturation" of the fracture network, i.e., the degree to which fracture location is dense enough to force fracture interactions during the growth process (Davy et al. 2010; Scholz 2002). A more saturated system will develop more uniform fracturing leading to higher fractal dimensions. This would indicate that our fracture network in Soultz and Basel are close to being saturated.

An important question concerns the constraints that an observed distribution of fracture intersection points along a borehole places on the scaling of the fracture network within the rock mass penetrated by the borehole. Clearly, the 1D distribution of fracture spacing along the hole reflects to some degree the characteristics of the 3D network (i.e., the parameters controlling fracture location (D_{3D}) and fracture length (a_{3D}) in the dual power-law model). Moreover, analyses of borehole data show that fracture spacing distributions are commonly fractal in nature and characterized by a fractal dimension, D_{1D}. Darcel et al. (2003b) derived stereological relationships for fractal DFNs which relate the D_{1D} values derived from scanlines through a DFN to the scaling parameters of fracture patterns on 2D surfaces within the DFN (i.e., the correlation dimension of fracture centers, D_{2D}, and the length exponent a_{2D}), and also to the 3D scaling parameters (D_{3D} and a_{3D}). Applying the relations to synthetic data, they found that the 3D spatial distribution of fractures could not be constrained from the lower-dimension scaling parameters, except when the length exponent was known. However, our stereological analysis shows that even when the fracture length exponent is known, it is not possible to deduce 3D scaling parameters from 1D data. The problem is strongly underdetermined and leads to non-unique solutions. Additional information must be included to circumvent these limitations. This can be done in the case of geothermal reservoir development by integrating the spatial distribution of induced seismicity (Afshari Moein et al. 2018b), although this information becomes available only after that reservoir stimulation has been performed. Another potential source of information stems from the in situ stress variations that are revealed by extensive wellbore failure that is commonly observed in deep boreholes (Afshari Moein et al. 2018a).

7 Conclusions

Fractal fracture networks that respect the dual power-law model of Davy et al. (1990) were generated using a Multiplicative Cascade process. Two scaling parameters inherent in the model relate to the distribution of distances between fracture centers (correlation dimension, D), and the distribution of fracture lengths (length exponent, a). Analyses of 1D synthetic fracture distributions along lines generated within the model the and deep borehole fracturing data show that correlation dimension obtained from the two-point correlation method provides the most stable and reliable estimate of the fractal dimension of fractures on 1D scanlines or boreholes. The spatial distributions of fractures along three deep boreholes in crystalline rock at Basel and Soultz-sous-Forêts was found to be fractal over more than two orders of magnitude in scale, and in all cases the fractal dimensions lay in the range 0.86–0.88. Fracture sets of common orientation within the wells were also fractal over more than 2 orders of magnitude, although the fractal dimension ranged between 0.65 and 0.75. This constitutes strong evidence that fracturing in rock masses penetrated by the wells follows a fractal organization.

Analyses performed on synthetic fractal fracture networks show that it is not possible to estimate the 2D and 3D fractal scaling parameters of correlation dimension or length exponent from the 1D correlation dimension of fracturing spacing from scanlines through the network. This was found to be true even if the length exponent of the fracture distribution was known a priori. The stereological problem of constraining scaling in 2D and 3D from 1D observations is too underdetermined and requires information in addition to the length exponent. A possible development of this research is to perform stereological analysis on DFNs generated using novel algorithms that respect the mechanical interactions between neighboring fractures. Further datasets from deep boreholes and underground laboratories will provide a valuable opportunity to test the methodologies developed in this paper.

Acknowledgements The research leading to these results received funding from the European Community's Seventh Framework Program under Grant agreement no. 608553 (Project IMAGE). We would like thank Simon Löw for his continuous support and constructive comments during this project. We are also thankful to the anonymous

reviewers, associate editor and the editor for their valuable suggestions that led to improvements of the manuscript.

References

Afshari Moein MJ (2018) Linkage between fracture network, stress heterogeneities and induced seismicity in deep geothermal reservoirs (Doctoral Dissertation). Zurich: ETH Zurich. https://doi.org/10.3929/ethz-b-000294223

Afshari Moein MJ, Somogyvári M, Valley B, Jalali M, Loew S, Bayer P (2018a) Fracture network characterization using stress-based tomography. J Geophys Res Solid Earth,123. https://doi.org/10.1029/2018JB016438

Afshari Moein MJ, Tormann T, Valley B, Wiemer S (2018b) Maximum magnitude forecast in hydraulic stimulation based on clustering and size distribution of early microseismicity. Geophys Res Lett 45:6907–6917. https://doi.org/10.1029/2018GL077609

Alghalandis YF, Dowd PA, Xu C (2013) The RANSAC method for generating fracture networks from micro-seismic event data. Math Geosci 45:207–224

Alghalandis YF, Dowd PA, Xu C (2015) connectivity field: a measure for characterising fracture networks. Math Geosci 47:63–83. https://doi.org/10.1007/s11004-014-9520-7

Allegre CJ, Lemouel JL, Provost A (1982) Scaling rules in rock fracture and possible implications for earthquake prediction. Nature 297:47–49. doi:https://doi.org/10.1038/297047a0

Baecher GB, Lanney NA (1978) Trace length biases in joint surveys. In: Proceedings of the 19th U. S. Symposium on Rock Mechanics, vol 1, pp 56–65

Baghbanan A, Jing LR (2007) Hydraulic properties of fractured rock masses with correlated fracture length and aperture. Int J Rock Mech Min Sci 44:704–719. https://doi.org/10.1016/j.ijrmms.2006.11.001

Bak P, Tang C, Wiesenfeld K (1988) Self-organized criticality. Phys Rev A Gen Phys 38:364–374

Barton CC (1995) Fractal analysis of scaling and spatial clustering of fractures. Fractals in the earth sciences. Springer, Berlin, pp 141–178

Barton CA, Zoback MD (1992) Self-similar distribution and properties of macroscopic fractures at depth in crystalline rock in the Cajon Pass Scientific Drill Hole. J Geophys Res Solid Earth (1978–2012) 97:5181–5200

Berkowitz B, Hadad A (1997) Fractal and multifractal measures of natural and synthetic fracture networks. J Geophys Res Solid Earth (1978–2012) 102(B6):12205–12218. https://doi.org/10.1029/97JB00304

Boadu FK, Long LT (1994) The fractal character of fracture spacing and RQD. Int J Rock Mech Min Sci Geomech Abstr 31(2):127 ± 134

Bonnet E, Bour O, Odling NE, Davy P, Main I, Cowie P, Berkowitz B (2001) Scaling of fracture systems in geological media. Rev Geophys 39:347–383. https://doi.org/10.1029/1999RG000074

Bour O, Davy P (1997) Connectivity of random fault networks following a power law fault length distribution. Water Resour Res 33:1567–1583

Bour O, Davy P (1999) Clustering and size distributions of fault patterns: Theory and measurements. Geophys Res Lett 26(13):2001–2004

Bour O, Davy P, Darcel C, Odling N (2002) A statistical scaling model for fracture network geometry, with validation on a multiscale mapping of a joint network (Hornelen Basin, Norway). J Geophys Res Solid Earth 107

Chilès J (1988) Fractal and geostatistical methods for modeling of a fracture network. Math Geol 20:631–654

Clemo T, Smith L (1997) A hierarchical model for solute transport in fractured media. Water Resour Res 33:1763–1783. https://doi.org/10.1029/97WR01005

Cowie P, Knipe R, Main I (1996) Scaling laws for fault and fracture populations-Analyses and applications-Introduction. J Struct Geol 18:R5–R11

Darcel C (2002) Corrélations dans les réseaux de fractures: caractérisation et conséquences sur les propriétés hydrauliques. Doctoral Dissertation. Université Rennes 1. Rennes

Darcel C, Bour O, Davy P (2003a) Cross-correlation between length and position in real fracture networks. Geophys Res Lett 30(12):1650. https://doi.org/10.1029/2003GL017174

Darcel C, Bour O, Davy P (2003b) Stereological analysis of fractal fracture networks. J Geophys Res. https://doi.org/10.1029/2002JB002091

Darcel C, Bour O, Davy P, De Dreuzy JR (2003c) Connectivity properties of two-dimensional fracture networks with stochastic fractal correlation. Water Resour Res 39(10)

Davy P (1993) On the frequency-length distribution of the San Andreas fault system. J Geophys Res Solid Earth 98:12141–12151

Davy P, Sornette A, Sornette D (1990) Some consequences of a proposed fractal nature of continental faulting. Nature 348:56–58

Davy, Le Goc R, Darcel C, Bour O, De Dreuzy J-R, Munier R (2010) A likely universal model of fracture scaling and its consequence for crustal hydromechanics. J Geophys Res Solid Earth 115

Davy P, Darcel C, Le Goc R, Munier R, Selroos JO, Ivars MD (2018) DFN, why, how and what for, concepts, theories and issues. In: 2nd international discrete fracture network engineering conference. American Rock Mechanics Association

Day-Lewis AD (2008) Characterization and modeling of in situ stress heterogeneity. (PhD thesis), Stanford University, California, USA

de Dreuzy J-R, Davy P, Bour O (2001) Hydraulic properties of two-dimensional random fracture networks following a power law length distribution: 1. Effective connectivity. Water Resour Res 37:2065–2078

de Dreuzy JR, Davy P, Bour O (2002) Hydraulic properties of two-dimensional random fracture networks following power law distributions of length and aperture. Water Resour Res 38

Deere DU, Deere DW (1988) The rock quality designation (RQD) index in practice. In: Kirakaldie L (ed) Rock classification systems for engineering purposes. ASTM special publication 984. American Society for Testing Materials, Philadelphia, pp 91–101

Dershowitz WS, Einstein HH (1988) Characterizing rock joint geometry with joint system models. Rock Mech Rock Eng 21:21–51. https://doi.org/10.1007/bf01019674

Dershowitz W, Lee G, Geier J, Hitchcock S, La Pointe P (1993) FracMan user documentation. Golder Associates Inc, Seattle

Dezayes C, Genter A, Valley B (2010) Structure of the low permeable naturally fractured geothermal reservoir at Soultz. CR Geosci 342(7–8):517–530

Dèzes P, Schmid SM, Ziegler PA (2004) Evolution of the European Cenozoic Rift System: interaction of the Alpine and Pyrenean orogens with their foreland lithosphere. Tectonophysics 389(1–2):1–33

Eshelby JD (1957) The determination of the elastic field of an ellipsoidal inclusion, and related problems. Proc R Soc Lond A 241(1226):376–396

Evans KF (2005) Permeability creation and damage due to massive fluid injections into granite at 3.5 km at Soultz: 2. Critical stress and fracture strength. J Geophys Res Solid Earth 110:B4

Evans KF, Genter A, Sausse J (2005) Permeability creation and damage due to massive fluid injections into granite at 3.5 km at Soultz: 1. Borehole observations. J Geophys Res Solid Earth 110:B4

Genter A, Evans KF, Cuenot N, Fritsch D, Sanjuan B (2010) Contribution of the exploration of deep crystalline fractured reservoir of Soultz to the knowledge of enhanced geothermal systems (EGS). CR Geosci 342:502–516. https://doi.org/10.1016/j.crte.2010.01.006

Gillespie P, Howard C, Walsh J, Watterson J (1993) Measurement and characterisation of spatial distributions of fractures. Tectonophysics 226:113–141

Häring MO, Schanz U, Ladner F, Dyer BC (2008) Characterisation of the Basel 1 enhanced geothermal system. Geothermics 37(5):469–495

Harthong B, Scholtès L, Donzé F-V (2012) Strength characterization of rock masses, using a coupled DEM–DFN model. Geophys J Int 191:467–480

Hentschel H, Procaccia I (1983) The infinite number of generalized dimensions of fractals and strange attractors. Physica D 8:435–444

Hirata T, Satoh T, Ito K (1987) Fractal structure of spatial distribution of microfracturing in rock. Geophys J Int 90:369–374. https://doi.org/10.1111/j.1365-246X.1987.tb00732.x

Kim TH (2007) Fracture characterization and estimation of fracture porosity of naturally fractured reservoirs with no matrix porosity using stochastic fractal models. PhD Thesis. Texas A&M University, Texas

La Pointe P (1988) A method to characterize fracture density and connectivity through fractal geometry. Int J Rock Mech Min Sci Geomech, vol 6. Elsevier, pp 421–429

Ledésert B, Dubois J, Genter A, Meunier A (1993) Fractal analysis of fractures applied to Soultz-sous-Forêts hot dry rock geothermal program. J Volcanol Geoth Res 57:1–17

Lei LQ, Gao K (2018) Correlation between fracture network properties and stress variability in geological media. Geophys Res Lett 45(9):3994–4006

Lei Q, Latham JP, Tsang CF, Xiang J, Lang P (2015) A new approach to upscaling fracture network models while preserving geostatistical and geomechanical characteristics. J Geophys Res Solid Earth 120:4784–4807

Lei Q, Latham JP, Tsang CF (2017) The use of discrete fracture networks for modelling coupled geomechanical and hydrological behaviour of fractured rocks. Comput Geotech 85:151–176

Lovejoy S, Schertzer D (1986) Scale invariance, symmetries, fractals, and stochastic simulations of atmospheric phenomena. Bull Am Meteorol Soc 67:21–32

Manning CE (1994) Fractal clustering of metamorphic veins. Geology 22:335–338

Meakin P (1991) Fractal aggregates in geophysics. Rev Geophys 29:317–354

Merceron T, Velde B (1991) Application of Cantor's method for fractal analysis of fractures in the Toyoha Mine, Hokkaido, Japan. J Geophys Res Solid Earth 96:16641–16650

Moein MJA, Valley B, Ziegler M (2016) Preliminary fractal analysis of fracture spacing inferred from an acoustic televiewer log run in the Basel-1 geothermal well (Switzerland). Rock mechanics and rock engineering: from the past to the future. CRC Press, London, pp 103–1107

Moller J, Waagepetersen RP (2003) Statistical inference and simulation for spatial point processes. Monographs on statistics and applied probability, vol 100. Chapman and Hall, UK

Odling (1992) Network properties of a two-dimensional natural fracture pattern. Pure Appl Geophys 138:95–114

Odling NE, Gillespie P, Bourgine B, Castaing C, Chiles JP, Christensen NP, Fillion E, Genter A, Olsen C, Thrane L, Trice R (1999) Variations in fracture system geometry and their implications for fluid flow in fractured hydrocarbon reservoirs. Pet Geosci 5:373–384

Pollard D, Segall P (1987) Theoretical displacements and stresses near fractures in rock: with applications to faults, joints, veins, dikes, and solution surfaces. Fract Mech Rock 277:277–349

Power WL, Tullis TE (1991) Euclidean and fractal models for the description of rock surface roughness. J Geophys Res Solid Earth 96:415–424

Renshaw CE (1999) Connectivity of joint networks with power law length distributions. Water Resour Res 35:2661–2670

Roy A, Perfect E, Dunne WM, McKay LD (2014) A technique for revealing scale-dependent patterns in fracture spacing data. J Geophys Res Solid Earth 119:5979–5986

Scholz CH (2002) The mechanics of earthquakes and faulting. Cambridge University press, New York

Sornette D (2006) Critical phenomena in natural sciences: chaos, fractals, selforganization and disorder: concepts and tools. Springer, Berlin

Sornette D, Davy P, Sornette A (1990) Structuration of the lithosphere in plate tectonics as a self-organized critical phenomenon. J Geophys Res Solid Earth 95:17353–17361

Spyropoulos C, Scholz CH, Shaw BE (2002) Transition regimes for growing crack populations. Phys Rev E 65:056105

Valley B (2007) The relation between natural fracturing and stress heterogeneities in deep-seated crystalline rocks at Soultz-sous-Forêts (France). Doctoral Dissertation. ETH Zürich, Zürich

Valley B, Evans K (2014) Preliminary assessment of the scaling relationships of in-situ stress orientation variations indicated by wellbore failure data. In: The 2014 ISRM European Rock Mechanics Symposium (EUROCK 2014). rock engineering and rock mechanics: structure in and on rock masses. CRC Press, Vigo, pp 463–468

Valley B, Dezayes C, Genter A (2007) Multiscale fracturing in the Soultz-sous-Forêts basement from borehole image analyses. In: Proceedings EHDRA scientific conference, 28. Soultz-sous-Forêts, France

Valley B, Jalali MR, Ziegler M, Evans KF (2014) Constraining DFN characteristics for deep geothermal projects by considering the effects of fractures on stress variability. In: International discrete fracture network engineering conference DFNE 2014. Vancouver, BC, Canada

Velde B, Dubois J, Touchard G, Badri A (1990) Fractal analysis of fractures in rocks: the Cantor's Dust method. Tectonophysics 179:345–352

Verscheure M, Fourno A, Chilès J-P (2012) Joint inversion of fracture model properties for CO2 storage monitoring or oil recovery history matching. Oil Gas Sci Technol Revue d'IFP Energies nouvelles 67:221–235

Watanabe K, Takahashi H (1993) Fractal characterization of subsurface fracture network for geothermal energy extraction system. In: Proceedings, eighteenth workshop on geothermal reservoir engineering, Stanford University, Stanford, CA. Report No. SGP-TR-145-17

Ziegler M, Valley B, Evans F (2015) Characterisation of nature fractures and fracture zones of the Basel EGS reservoir inferred from geophysical logging of the Basel-1 well. In: Proceedings world geothermal congress 2015, Melbourne, Australia